






Beta-Particle Transport and Thermalization in Kilonova Ejecta with Detailed Atomic Microphysics

Zachary L. Andelman ^{1,2*}, Christopher L. Fryer ^{2,3,4}, Christopher J. Fontes ^{2,5},
Matthew R. Mumpower ^{7,2,6,8}, and Ryan T. Wollaeger ^{2,6}

¹*Department of Astrophysical Sciences, Princeton University, 4 Ivy Lane, 08540, Princeton, NJ, USA*

²*Center for Theoretical Astrophysics, Los Alamos National Laboratory, Los Alamos, NM 87545, USA*

³*Theoretical Division, Los Alamos National Laboratory, Los Alamos, NM 87545, USA*

⁴*Department of Physics, The George Washington University, Washington, DC 20052, USA*

⁵*Computational Physics Division, Los Alamos National Laboratory, Los Alamos, NM 87545, USA*

⁶*Computing and Artificial Intelligence Division, Los Alamos National Laboratory, Los Alamos, NM 87545, USA*

⁷*Obsidian Research, Fort Wayne, IN 46835, USA*

⁸*Department of Physics and Astronomy, University of Notre Dame, Notre Dame, IN, 46656, USA*

Accepted XXX. Received YYY; in original form ZZZ

ABSTRACT

When two neutron stars collide, they eject material containing heavy nuclei formed by the rapid neutron capture process (r -process). As these nuclei decay, they power a bright optical/near-infrared transient known as a kilonova (KN). Modeling KN emission is a complex problem involving atomic opacities, radiation transport, and heating powered by the thermalization of radioactive decay products like γ -rays, α -particles, and β -particles. For heating by γ -rays, many KN modeling codes do full radiation transport calculations. However, heating by α - and β -particles relies on simplified descriptions of collisions and transport, and remains an important source of uncertainty in KN models. In this paper, we study the thermalization and transport of β -particles. To study thermalization, we use evaluated atomic physics data to estimate per-species contributions to energy deposition, scattering, and electron impact ionization, which we make available online. To include non-local effects, we develop a fully relativistic framework for charged particle transport in a spherically symmetric, homologously expanding ejecta, considering two limiting magnetic-field geometries. Non-local energy deposition and escape reduce thermalization efficiency, especially in the innermost and outermost ejecta, lowering the ejecta temperature and ionization state compared to local deposition models. Coulomb scattering partially offsets these effects by trapping particles at intermediate times. Ionization by secondary electrons significantly enhances the overall ionization rate. We provide analytic prescriptions for the spatially dependent thermalization efficiency for use in future light-curve calculations. Our results demonstrate that evaluated atomic data and charged-particle transport should be incorporated into the next generation of KN models.

Key words: transients: neutron star mergers – atomic data – methods: numerical

1 INTRODUCTION

In binary neutron star (BNS) mergers and some black hole-neutron star mergers, the radioactive decay of heavy nuclides produced by the rapid neutron capture process (r -process) powers a bright flare in the optical and near-infrared (IR) known as a kilonova (KN) (Li & Paczyński 1998; Metzger et al. 2010), accompanied by a short gamma ray burst (GRB) (Paczynski 1986; Eichler et al. 1989; Narayan et al. 1992) and gravitational waves (GWs). The first confirmed KN, the bright optical transient AT 2017gfo, was discovered in association with gravitational wave event GW170817 (Abbott et al. 2017b) and the short GRB 170817A (Goldstein et al. 2017; Savchenko et al. 2017), providing compelling evidence that BNS mergers are sites of r -process nucleosynthesis (Pian et al. 2017; Tanvir et al. 2017).

The multi-band, multi-messenger nature of these events makes

them a powerful astrophysical tool for constraining cosmological parameters (Nissanke et al. 2013; Abbott et al. 2017a), binary star evolution models (Fong & Berger 2013; Fong et al. 2022), cosmic nucleosynthesis models (Kasen et al. 2017; Côté et al. 2018; Rosswog et al. 2018), the physics of the r -process, and the equation of state for dense nuclear matter (Bauswein et al. 2013; Margalit & Metzger 2017).

The r -process is expected to operate in material ejected from the system dynamically (Lattimer & Schramm 1974; Freiburghaus et al. 1999; Rosswog et al. 1999; Goriely et al. 2011; Korobkin et al. 2012) or unbound from the remnant accretion disk by neutrino-driven (Dessart et al. 2009; Perego et al. 2014; Radice et al. 2018) or viscously-driven (Nedora et al. 2019, 2021) wind (for a review, see Rosswog & Korobkin 2024). The ejecta are heated and ionized by the thermalization of radioactive decay products like β -particles, α -particles, γ -rays, and fission fragments (Barnes et al. 2016).

The observed light curves and spectra depend on the ejecta density

* E-mail: zack.andelman@princeton.edu

and velocity structure, ejecta morphology, wavelength-dependent opacity, and radioactive heating rate (Metzger et al. 2010; Roberts et al. 2011; Kasen et al. 2017; Tanaka et al. 2017; Wollaeger et al. 2018; Bulla 2019; Even et al. 2020; Hotokezaka & Nakar 2020; Kawaguchi et al. 2020; Korobkin et al. 2021; Wollaeger et al. 2021; Fryer et al. 2024). Both the opacity and heating rate are sensitive to nuclear physics models (Barnes et al. 2021), ejecta composition, and the efficiency of decay product thermalization, since the decay energy may escape or be lost by adiabatic expansion (Barnes et al. 2016; Kasen & Barnes 2019).

The ejecta composition also affects the opacity — especially lanthanide elements due to their valence f -shell electrons (Barnes & Kasen 2013; Kasen et al. 2013; Tanaka & Hotokezaka 2013; Wollaeger et al. 2018; Fontes et al. 2020, 2026). The opacity is additionally sensitive to the ejecta ionization and excitation structure (Pognan et al. 2022b, 2023; Banerjee et al. 2025; Pognan et al. 2025).

The thermalization efficiency is a key uncertainty because it depends on the interactions between radioactive decay products and the ejecta, for which the relevant atomic data are often unavailable despite ongoing work (Kasen et al. 2013; Fontes et al. 2015, 2020; Pognan et al. 2022a). Since decay products can travel significant distances in the ejecta before depositing their energy, thermalization also depends on charged-particle transport, and therefore on the magnetic field, whose geometry is largely unconstrained (Barnes et al. 2016).

The ionization structure is subject to similar uncertainties. During the nebular phase, the ejecta are primarily ionized by non-thermal decay products (Hotokezaka et al. 2021; Pognan et al. 2022a; Brethauer et al. 2026), so the ionization rate depends both on thermalization and impact ionization cross sections. Recombination is dominated by the atomic process known as dielectronic capture, whose rates are sensitive to fine-structure effects (Hotokezaka et al. 2021; Banerjee et al. 2025; Singh et al. 2025).

In the present work, we focus on β -particles, which carry most of the decay energy, and revisit their thermalization and transport. Building on previous thermalization efficiency calculations (Barnes et al. 2016; Hotokezaka et al. 2016; Kasen & Barnes 2019; Waxman et al. 2019; Hotokezaka & Nakar 2020; Van den Berg & Hotokezaka 2026), we incorporate evaluated atomic physics data and estimate per-species contributions to energy deposition and electron impact ionization. We also estimate per-species contributions to scattering, whose role in particle transport has previously been neglected. We combine these data using abundance patterns generated from our nuclear network calculations, but we make our atomic data available online for use with arbitrary compositions.

Despite the importance of thermalization, explicit charged-particle transport has only been considered by a few KN studies (Barnes et al. 2016, 2021; Wollaeger et al. 2024). We build on this work by developing a fully relativistic framework for particle transport in a spherically symmetric, homologously expanding ejecta, and by including an expanded set of microphysical phenomena.

We consider two limiting transport scenarios: no transport, corresponding to highly tangled or toroidal magnetic fields, and maximal transport, corresponding to weak or coherent radial magnetic fields. We investigate the effect of non-local energy deposition on the spatially dependent thermalization efficiency and ionization balance. We provide analytic prescriptions for the spatially dependent thermalization efficiency for use in future light curve calculations.

This paper is structured as follows. In Section 2, we describe our approach to microphysical processes, including r -process yields, decay spectra, and electron-atom interactions. In Section 3, we describe our idealized global ejecta and particle transport model. In

Section 4, we show the results of our global model calculations and explore their implications for thermalization and ionization structure. We conclude in Section 5.

2 MICROPHYSICS

2.1 Nuclear yields

In the seconds after the BNSM, the high temperature and neutron flux creates the necessary conditions for r -process nucleosynthesis (Miller et al. 2019). Using the nuclear reaction network code PRISM (Sprouse et al. 2021), we calculate nuclear yields for three thermodynamic trajectories taken from tracer particles in 3D hydrodynamic simulations. Our strong r -process trajectory comes from a relativistic hydrodynamics simulation of a BNSM in Goriely et al. (2011) with an electron fraction $\simeq 0.1$, as expected for BNSM dynamical ejecta. Our medium and weak r -process trajectories come from general relativistic neutrino radiation magnetohydrodynamics simulations of black hole accretion in Sprouse et al. (2024) using electron fractions $\simeq 0.2$ and 0.4 respectively, as expected for BNSM disk winds.

The nuclides produced by the r -process proceed towards the valley of stability via β^- -decay processes of the form



where Z is the atomic number, A is the mass number, and ${}^A_Z X$ is an isotope of element X . β decays produce an electron anti-neutrino and a high-energy electron, or β -particle. If the daughter nuclide is in an excited nuclear state, it can additionally emit γ -rays or neutrons as it de-excites.

The r -process preferentially synthesizes nuclides near specific mass numbers $A \sim 80, 130, \text{ and } 195$, known as r -process peaks, where neutron-rich nuclei exhibit enhanced stability due to closed nuclear shells. In Figure 1, we plot the elemental abundances of our three r -processes at 30 days post-merger. Our weak r -process yields only first peak elements ($Z \sim 40, A \sim 80, \mu_{\text{mmw}} \simeq 42$), where μ_{mmw} is the mean molecular weight, ignoring free electrons. Our medium r -process yields nuclei up to and around Te ($Z = 52, A \sim 130, \mu_{\text{mmw}} \simeq 115$). Our strong r -process yields both third peak nuclei and actinides.

Our strong and weak r -processes produce a significant number of α particles ($Z = 2$). In the strong scenario, this is due to the production of α particles from the decay of actinide species (Lund et al. 2023). In the weak scenario, this is instead due to the conversion of neutrons and protons into α particles during the early stages of nucleosynthesis (McLaughlin et al. 1996).

Feng et al. (2026) recently showed that r -process yields may be sensitive to magnetically powered outbursts from long-lived merger remnants. Shocks increase the electron fraction by heating the ejecta, which accelerates weak reactions like positron capture on neutrons, suppressing 3rd-peak production. However, they also increase the ejecta entropy, enhancing heavy element production. The final abundances are therefore still highly uncertain, motivating our choice to consider a range of abundance patterns.

2.2 β decay spectra

For each nuclide, we source β decay rates and branching ratios from the International Atomic Energy Agency (IAEA) Livechart¹.

¹ www-nds.iaea.org/relnsd/vcharthtml/VChartHTML.html

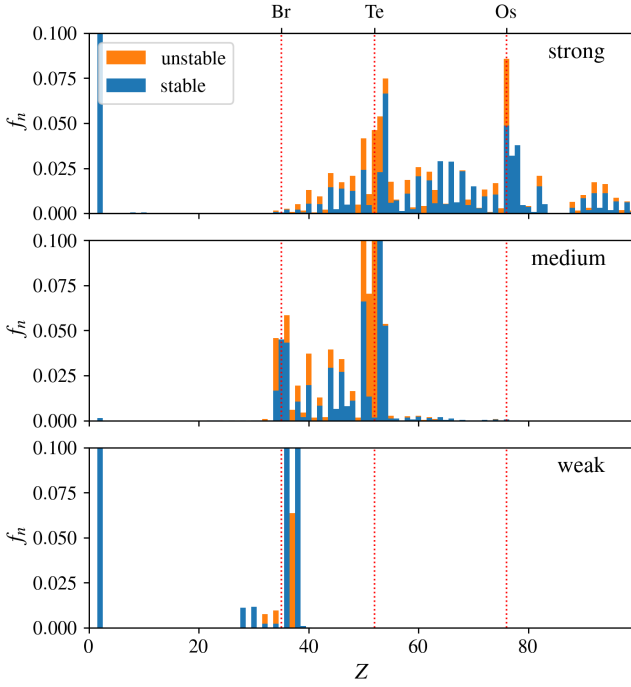


Figure 1. Elemental number fractions at 30 days post-merger for our strong (top panel), medium (middle panel), and weak (bottom panel) r -processes. Each element is partitioned into stable (blue) and unstable (orange) isotopes. Bromine ($Z = 35$), Tellurium ($Z = 52$), and Osmium ($Z = 76$) are marked by vertical, red-dotted lines as representatives of the r -process peaks. Our weak r -process yields only first-peak elements. Our medium r -process yields nuclei up to and around Te. Our strong r -process yields both third-peak nuclei and actinides.

Livechart data is directly sourced from the Evaluated Nuclear Structure Data File (ENSDF)², which is compiled from a review of available experimental data supplemented with systematic trend studies and theoretical models.

We compute β decay spectra from the coupled Quasiparticle Random Phase Approximation and Hauser-Feshbach (QRPA+HF) model (Mumpower et al. 2016; Möller et al. 2019; Mumpower et al. 2025). The model occasionally fails for nearly stable nuclei because there is little energy available for β decay, so small errors in the nuclear level states can produce large errors in the decay spectrum. In these cases, we fall back to the β decay spectra in Livechart, which are computed with the code BETA SHAPE (Mougeot 2015a,b).

For each nuclide, the specific decay rate (units $\text{s}^{-1}\text{g}^{-1}$) is

$$\Gamma_{\text{dec}} = N_A [(\ln 2)Yb\tau_h^{-1} + \dot{Y}_{\text{dec}}], \quad (2)$$

where N_A is Avogadro’s number, Y is the isotopic abundance (units mol/g), b is the β^- decay branching ratio, τ_h is the half-life, and \dot{Y}_{dec} is the rate of change in the abundance due to β^- decay. Most r -process nuclides have branching ratios of unity, but a handful have other significant decay pathways.

Most nuclei follow isochronic decay pathways, i.e. they decay into nuclides with longer half-lives (Sprouse et al. 2022). This lets abundances reach a quasi-steady-state between feeding and decay, so the first term in Equation 2 dominates. However, non-isochronic decays produced by fission and some actinides cause some nuclei

abundances to change rapidly, so the second term in Equation 2 must be accounted for.

Let $dn^{(Z,A)}(E)$ denote the number of β -particles produced at infinitesimal energy bin dE by nuclide (Z, A) . These spectra are normalized to unity, the number of β particles produced per decay, following nuclear physics conventions. The total decay spectrum (units $\text{s}^{-1}\text{g}^{-1}\text{erg}^{-1}$) is the sum of contributions from each nuclide,

$$d\lambda_{\text{dec}}(E) = \sum_{Z,A} \Gamma_{\text{dec}}^{(Z,A)} dn^{(Z,A)}(E). \quad (3)$$

For our strong r -process at 30 day post-merger, there are 339 distinct unstable nuclei with nonzero abundances. We compute decay spectra for 287 nuclei and use the Livechart spectra for 40 nuclei. No spectra are available for the remaining 12 nuclei, but they produce a negligible fraction of the decay electrons ($< 10^{-6}$ of the decay rate), so they can be neglected.

In Figure 2, we plot the β decay and energy injection rates and the mean β -particle energy for our three r -processes. The energy injection rates drop rapidly as nuclides reach the line of β stability, and can be approximated by the following power laws:

$$\begin{aligned} Q_{\text{inj}}^{(\text{strong})} &\sim 5.63 \times 10^9 t_d^{-1.31} \text{ erg s}^{-1}\text{g}^{-1} \\ Q_{\text{inj}}^{(\text{medium})} &\sim 5.43 \times 10^9 t_d^{-1.28} \text{ erg s}^{-1}\text{g}^{-1} \\ Q_{\text{inj}}^{(\text{weak})} &\sim 1.00 \times 10^8 t_d^{-1.14} \text{ erg s}^{-1}\text{g}^{-1}, \end{aligned} \quad (4)$$

where t_d is the time in days. We compute the power law prefactor and exponent using a least-squares linear regression in log space. For our strong r -process, the power law exponent is consistent with previous works, which find values ranging from -1.4 to -1.1 (Metzger et al. 2010; Goriely et al. 2011; Roberts et al. 2011; Korobkin et al. 2012; Hotokezaka et al. 2017).

The strong and medium r -processes have similar decay energies, but the weak r -process is less energetic by a factor ~ 50 . The mean β -particle energy decreases gradually from around 0.8 MeV at early times to around 0.2 MeV at late times. For all r -processes, the non-steady-state term contributes significantly to the decay rate.

In Figure 3, we plot the normalized β spectra for our three r -processes at various times. We also list the three nuclides that contribute most to the decay at 1, 10, 30, and 100 days post-merger. At 0.01 days, the β decay spectra peak at ~ 1 MeV. Over time, the spectra shift to lower energies because higher-energy decays are generally associated with shorter-half-life nuclides. At each time, the spectra are dominated by contributions from only a handful of nuclides, producing lumpy features.

We do not account for long-lived nuclear isomers of parent nuclides, such as those of ^{128}Sb and ^{85}Kr . In these cases, the isomer may contribute significantly to the β spectrum at late times after the ground state nuclides have decayed (Misch et al. 2021a,b; Misch & Mumpower 2024). Future work should investigate whether this effect can significantly modify the decay spectrum and, if so, under what conditions.

2.3 Electron-atom interactions

Suprathermal β -particles can undergo many interactions with the atoms of the background plasma, including

- (i) Electron impact ionization (EII): an energetic electron interacts with an atom and produces an ion and a secondary electron;
- (ii) Electron impact excitation (EIE): an energetic electron interacts with an atom and promotes the atom to an excited state;

² www.nndc.bnl.gov/ensdf/

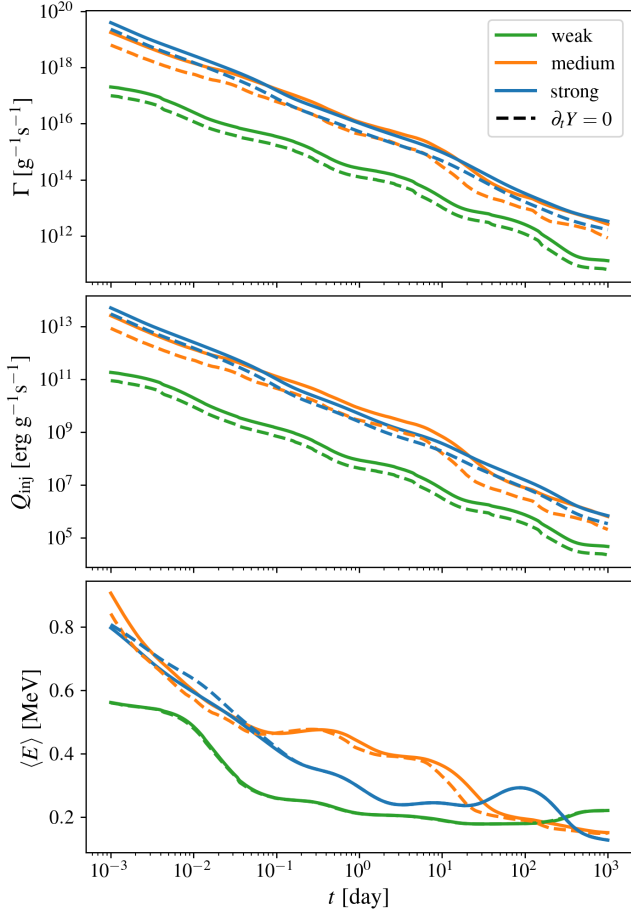


Figure 2. The β decay rate (top panel), the β energy injection rate (middle panel), and the mean β -particle energy (bottom panel) as a function of time for our strong (blue), medium (orange), and weak (green) r -processes. The dashed lines show the contribution from only the steady-state term (Eq. 2). The energy injection rates drop rapidly as nuclides reach the line of β stability, and can be approximated by power laws. The non-steady-state term contributes significantly to the decay rate for all r -processes.

(iii) Electron-atom bremsstrahlung: an electron interacts with an atom via Coulomb forces, producing a photon;

(iv) Mott scattering: an electron interacts with an atom via Coulomb forces, resulting in elastic scattering.

We assume that scattering is dominated by (iv), so we ignore scattering contributions from (i)–(iii). For energy loss, we work in the continuous slowing-down approximation (CSDA), approximating discrete electron-atom interactions as a continuous stopping cross section given by

$$S(E) = \int d(\Delta E) \Delta E \frac{d\sigma(E)}{d\Delta E}, \quad (5)$$

where $d\sigma(E)/d\Delta E$ is a differential cross section in energy loss ΔE . The corresponding energy loss rate is $-dE/dt = nvS(E)$, where n is the target number density and v is the β -particle velocity.

CSDA is a good approximation for EII and EIE, but less so for bremsstrahlung, where the energy loss is dominated by rare interactions that consumes a significant fraction of the incident electron’s kinetic energy. However, in the following sections we show that the

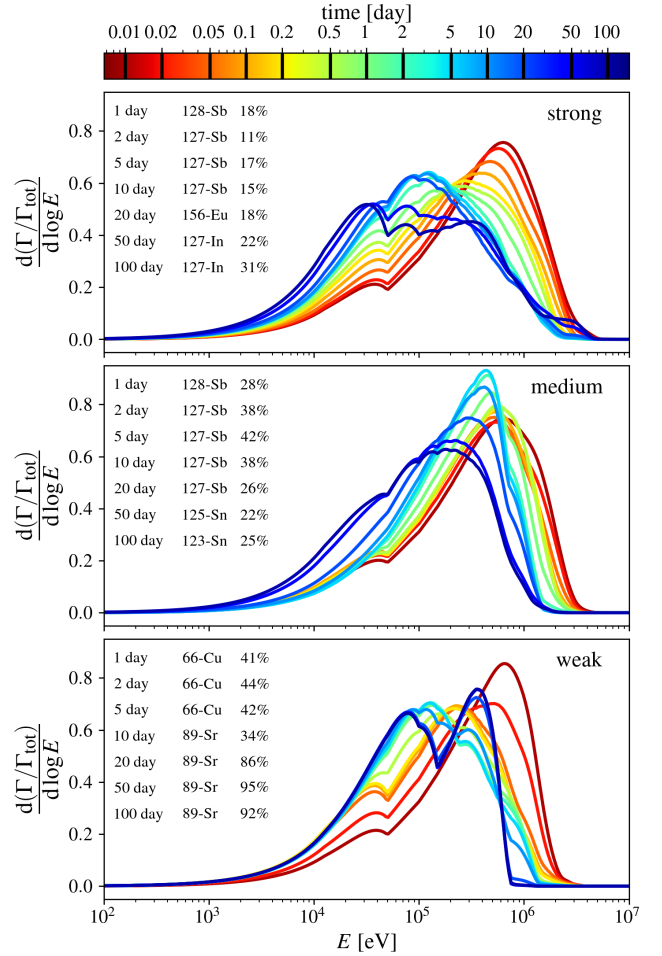


Figure 3. The β decay spectra as a function of time for our strong (top panel), medium (middle panel), and weak (bottom panel) r -processes. Each time is shown in a different color indicated by the colorbar. At various times, we indicate the nuclide with the largest contribution to the energy injection rate and its fractional contribution to the energy. At one day, the β decay spectra peak at ~ 1 MeV. Over time, the spectra shift to lower energies because higher-energy decays are generally associated with shorter-half-life nuclides. At each time, the spectra are dominated by contributions from only a handful of nuclides, producing lumpy features.

bremsstrahlung contribution to the energy loss is subdominant at the typical stopping cross sections.

For scattering (iv), the differential cross section diverges at small angles. Rather than modeling many small-angle scatters, we model scattering as isotropic using the transport (momentum-transfer) cross section given by

$$\sigma_t = \int d\mu_s (1 - \mu_s) \frac{d\sigma(E)}{d\mu_s}, \quad (6)$$

where $d\sigma(E)/d\mu_s$ is a differential cross section in cosine scattering angle μ_s . The corresponding mean free path is $\lambda_{\text{mfp}} = 1/(n\sigma_t)$.

The integrals in Equations 5 and 6 require evaluating differential cross sections at arbitrary electron energies. For tabulated data, this procedure requires interpolating between tabulated distributions. We use the method of quantile functions described in Appendix A.

2.3.1 The EEDL database

We model electron-atom interactions using data from the Electron-Photon Intersection Cross Sections database, version 2023 (EPICS2023), which is freely available online.³ We use the Evaluated Electron Data Library (EEDL) (Cullen 2017), one of the three datasets in the database. The EEDL dataset includes cross section and energy loss data for interactions between electrons and atoms with atomic numbers in the range 1 to 100. The data are given in the Evaluated Nuclear Data File (ENDF) format (Trkov & Brown 2018), which we parse into a json file using a PYTHON script.

The warm temperatures $\gtrsim 10^3$ K and magnetic fields $\sim 10^{-6}$ G in KN ejecta are different than the cold, unmagnetized atoms for which the EEDL dataset was constructed. However, lacking an equivalent dataset more tailored for astrophysical applications, we argue that the EEDL data is a reasonable approximation for our application.

First, the magnetic fields are too weak to significantly affect the atomic physics. At 10^{-6} G, the typical Zeeman energy shift is 10^{-14} eV. Second, the β -particles are much hotter than the ejecta, so we can neglect the thermal motion of the atoms and approximate the center-of-mass frame for each electron-atom interaction by the local fluid reference frame.

KN ejecta are also expected to be lightly ionized by the β -particles, especially in the nebular phase (Hotokezaka et al. 2021; Pognan et al. 2022a; Brethauer et al. 2026; Chiba et al. 2026), but the EEDL database only includes neutral targets. In the following sections, we discuss corrections to the neutral atom cross sections in the EEDL database to account for the ejecta ionization.

2.3.2 Electron impact ionization

EEDL includes the EII cross section and secondary electron spectrum as a function of primary electron energy for each electron subshell nlj of each element. The energy lost by the primary electron is the sum of the energy of the secondary electron and the subshell binding energy, $\Delta E = E_{\text{sec}} + I$, where I is the binding energy.

We adjust the neutral EII cross section for ionized targets using the empirical Lotz scaling (Bethe 1930; Lotz 1967). The EII cross section for subshell nlj and ionization stage q is related to the neutral cross section by

$$\sigma_{\text{EII},i,nlj}(E) = \frac{w_{q,nlj}}{w_{0,nlj}} \left(\frac{I_{0,nlj}}{I_{q,nlj}} \right)^2 \sigma_{\text{EII},0,nlj} \left(\frac{I_{q,nlj}}{I_{0,nlj}} E \right), \quad (7)$$

where $w_{q,nlj}$ and $I_{q,nlj}$ are the occupation number and binding energy respectively for subshell nlj and ionization stage q . The ratio of ionization potentials in the argument of the neutral cross section ensures that the cross sections are related at equivalent energies in threshold units. We approximate the subshell ionization potentials with energy eigenvalues, invoking Koopmans' theorem (Koopmans 1934). We compute these eigenvalues using the Hartree-Fock method implemented in the CATS code from Los Alamos, an adaptation of the atomic structure codes developed by Cowan (1981).

In Figure 4, we show the EII cross sections as a function of electron energy, and the subshell binding energies as a function of ionization stage q for Iron ($Z = 26$), Tellurium ($Z = 52$), and Uranium ($Z = 92$). The EII cross section at ion stage q is smaller than its neutral value by a factor $\sim q^2$, although the precise energy-dependent adjustment has a more complex dependence on the atomic structure.

For a given subshell, the binding energy increases with ionization

stage. We account for the extra energy by increasing the energy loss of the primary electron, while leaving the secondary electron distribution unchanged. This additive correction generally has a small effect on the EII stopping cross sections compared to the multiplicative correction from Equation 7.

2.3.3 Electron impact excitation

EEDL includes the EIE cross section and energy loss as a function of electron energy for each element. In principle, the EIE cross sections should also be modified as a function of target ionization stage. However, EEDL does not partition the EIE cross section by subshell, so we cannot apply a scaling relation as we did for the EII cross sections. In a later section, we show that, at the relevant β -particle energies, the EIE stopping cross section contribution is subdominant relative to the EII contribution, so the change in EIE cross sections can be neglected.

2.3.4 Electron-atom bremsstrahlung

The EEDL database includes the electron-atom bremsstrahlung cross section and average energy loss as a function of electron energy for each element. We apply these data to lightly ionized ejecta without modification. At impact parameters smaller than the atomic radius, this choice is justified because the missing electrons are spatially extended, so their absence does not significantly modify the Coulomb field probed by the β -particle.

At impact parameters larger than the atomic radius, the contribution to the stopping cross section is subdominant. We can demonstrate this behavior heuristically by comparing analytic expressions for stopping cross section in the limits of no screening (ns) and full screening (fs) (Bethe & Heitler 1934; Koch & Motz 1959), i.e.

$$S_{\text{brem,ns}} = 4r_0^2 \alpha q^2 \left[\ln(2\gamma) - \frac{1}{3} \right] \cdot E \quad (8)$$

$$S_{\text{brem,fs}} = 4r_0^2 \alpha q^2 \left[\ln \left(\frac{4}{3} \alpha^{-1} Z^{-1/3} \right) + \frac{1}{18} \right] \cdot E, \quad (9)$$

where $r_0 \equiv e^2/E_t$ is the classical electron radius, $E_t = m_e c^2$ is the electron rest-mass energy, $\alpha \equiv e^2/\hbar c$ is the fine-structure constant, $\gamma \equiv (1 - \beta^2)^{-1/2}$ is the particle Lorentz factor, $\beta \equiv v/c$, and these expressions are derived under the Born approximation in the ultra-relativistic limit.

Equation 8 represents the stopping cross section for a bare nucleus with charge q , which is limited by the maximum impact parameter set by the photon formation length. Equation 9 represents the stopping cross section for a neutral atom with nuclear charge q , which is limited by the maximum impact parameter set by the atomic radius. For $E \lesssim 70 Z^{-1/3}$ MeV, which is satisfied for typical β -particle decay energies, the ns cross section is less than the fs cross section, so the photon formation length provides a more restrictive cutoff than the atomic radius and the large impact parameter contribution can be neglected.

2.3.5 Mott scattering

The EEDL database includes the differential Mott scattering cross section as a function of electron energy. By our arguments in the previous subsection, the stopping cross section contribution at impact parameters smaller than the atomic radius is insensitive to target ionization.

³ www.nds.iaea.org/epics/

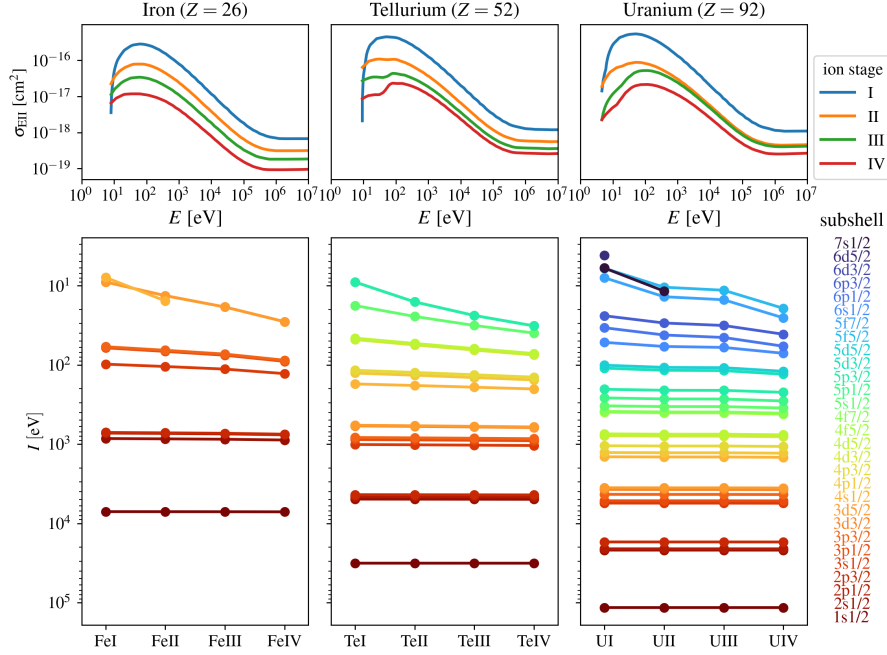


Figure 4. EII cross sections as a function of electron energy (top row) and subshell binding energies as a function of ionization stage (bottom row) for Iron ($Z = 26$) (first column), Tellurium ($Z = 52$) (second column), and Uranium ($Z = 92$) (third column). In the top row, each ionization stage is shown in a different color, indicated by the legend. In the bottom row, each subshell is shown in a different color indicated by the annotations on the right side of the plot. For an ion stage q , the EII cross section is smaller than its neutral value by a factor $\sim q^2$, although the precise energy-dependent adjustment to the cross section has a more complex dependence on the atomic structure.

For ionized targets, long-range Coulomb forces produce a small-angle scattering contribution that must be accounted for. In the limit of small $1 - \mu_s$, where μ_s is the cosine of the scattering angle, the Mott scattering differential cross section for a target element i is

$$\frac{d\sigma_{\text{mott}}}{d\mu_s} \approx 2\pi \bar{q}_i^2 \left(\frac{r_0}{\gamma\beta^2} \right)^2 \frac{1}{(1 - \mu_s)^2}, \quad (10)$$

where \bar{q}_i^2 is the average square ionization stage of element i . The integrated cross section is

$$\sigma_{\text{mott}}(\mu_s) = \int_{-1}^{\mu_s} d\mu'_s \frac{d\sigma_{\text{mott}}}{d\mu'_s} \approx 2\pi \bar{q}_i^2 \left(\frac{r_0}{\gamma\beta^2} \right)^2 \frac{1}{1 - \mu_s}. \quad (11)$$

The scattering angle associated with impact parameter b is given by setting the geometric area πb^2 equal to the integrated cross section $\sigma_{\text{mott}}(\mu_s)$ and solving for μ_s , which gives

$$1 - \mu_s \approx \frac{2}{b^2} \left(\frac{r_0}{\gamma\beta^2} \right)^2. \quad (12)$$

Small-angle scattering is produced by impact parameters from the atomic radius to the Debye length, given by

$$\lambda_D = \left(\frac{k_B T}{4\pi e^2 n_i (\bar{q} + \bar{q}^2)} \right)^{1/2} \approx 2.2 T_3^{1/2} n_{i,4}^{-1/2} (\bar{q} + \bar{q}^2)^{-1/2} \text{ cm}, \quad (13)$$

where $T_3 = T/10^3$ K is the temperature, $n_{i,4} = n_i/10^4 \text{ cm}^{-3}$ is the ion number density, and \bar{q} and \bar{q}^2 are the average ionization stage and square ionization stage across all elements. We have included the contribution of free electrons, whose number density is $\bar{q}n_i$. On scales $\gtrsim \lambda_D$, the Coulomb potential of the ion is effectively screened by polarization of the ejecta and the associated redistribution of charge.

Computing the transport cross section (Eq. 6) for the Mott differential cross section (Eq. 10) and integrating over the allowed impact parameters gives

$$\begin{aligned} \sigma_{t,\text{Mott}} &= 4\pi \bar{q}_i^2 \left(\frac{r_0}{\gamma\beta^2} \right)^2 \ln \Lambda_{\text{sa}} \\ &\approx 1.0 \times 10^{-24} \bar{q}_i^2 \gamma^{-2} \beta^{-4} \ln \Lambda_{\text{sa}} \text{ cm}^2, \end{aligned} \quad (14)$$

where $\ln \Lambda_{\text{sa}} = \ln(\lambda_D/r_{\text{atom}}) \approx \ln \Lambda - 6.8 + (1/3) \ln Z$ is the small-angle Coulomb logarithm, which we define in relation to the total Coulomb logarithm

$$\ln \Lambda = \ln \left(\frac{\lambda_D}{\lambda_C} \right) \approx 22.9 + \frac{1}{2} \ln \left(\frac{T_3}{n_{i,4} (\bar{q} + \bar{q}^2)} \right), \quad (15)$$

where $\lambda_C = h/m_e c$ is the electron Compton wavelength.

2.4 Møller scattering

In addition to Coulomb interactions with atoms and ions, β -particles also lose energy through Coulomb interactions with free thermal electrons. The differential cross section for electron-electron scattering, or Møller scattering, has an analytic form from quantum field theory given by (Møller 1932; Itzykson & Zuber 1980, Eq. 6-42)

$$\begin{aligned} \frac{d\sigma_{\text{mol}}}{d\Omega_{\text{cm}}} &= \frac{e^4 (2\mathcal{E}_{\text{cm}}^2 - E_r^2)^2}{4\mathcal{E}_{\text{cm}}^2 (\mathcal{E}_{\text{cm}}^2 - E_r^2)^2} \\ &\left[\frac{4}{\sin^4 \theta_{\text{cm}}} - \frac{3}{\sin^2 \theta_{\text{cm}}} + \frac{(\mathcal{E}_{\text{cm}}^2 - E_r^2)^2}{(2\mathcal{E}_{\text{cm}}^2 - E_r^2)^2} \left(1 + \frac{4}{\sin^2 \theta_{\text{cm}}} \right) \right], \end{aligned} \quad (16)$$

where $\mathcal{E} = E + E_r$ is the total electron energy and the subscript “cm” indicates that a quantity is measured in the center-of-mass (CM)

frame. The Lorentz factors in the CM and local fluid frames are related by (Møller 1932, Eq. 67),

$$\gamma_{\text{cm}} = \sqrt{(1/2)(\gamma + 1)}. \quad (17)$$

Using Equation 17 to write \mathcal{E}_{cm} in terms of the fluid frame Lorentz factor, we recast Equation 16 in the following form,

$$\frac{d\sigma_{\text{mol}}}{d\mu_{\text{s,cm}}} = 4\pi \left(\frac{r_0}{\gamma\beta} \right)^2 \frac{\gamma + 1}{\beta^2} \left[\frac{4}{(1 - \mu_{\text{s,cm}}^2)^2} - \frac{3}{1 - \mu_{\text{s,cm}}^2} + \frac{(\gamma - 1)^2}{4\gamma^2} \left(1 + \frac{4}{1 - \mu_{\text{s,cm}}^2} \right) \right]. \quad (18)$$

The scattering angles in the CM and fluid frames are related by a Lorentz boost via (Møller 1932, Eq. 68)

$$\mu_{\text{s,cm}} = \frac{\mu_{\text{s}}^2 - \gamma_{\text{cm}}^2(1 - \mu_{\text{s}}^2)}{\mu_{\text{s}}^2 + \gamma_{\text{cm}}^2(1 - \mu_{\text{s}}^2)} = \frac{2 - (\gamma + 3)(1 - \mu_{\text{s}}^2)}{2 + (\gamma - 1)(1 - \mu_{\text{s}}^2)}. \quad (19)$$

The inverse relation is given by

$$\mu_{\text{s}}^2 = \frac{(1 + \gamma)(1 + \mu_{\text{s,cm}})}{(1 + \gamma)(1 + \mu_{\text{s,cm}}) + 2(1 - \mu_{\text{s,cm}})}. \quad (20)$$

In the CM frame, the two electrons produced by a Møller scattering interaction are identical, producing the forward-backward symmetry in the differential cross section. In other words, an electron is equally likely to scatter forwards or backwards in the CM frame. In the fluid frame, the forward-scattered electron has more energy than the backward-scattered electron. To ensure that we always follow the higher-energy electron, we multiply the differential cross section by two and restrict its domain to $\mu_{\text{s,cm}} > 0$. It follows that the energy loss in the local fluid frame is at most half the electron energy. Doing a Lorentz boost, the precise formula is

$$\Delta E/E = (1/2)(1 - \mu_{\text{s,cm}}). \quad (21)$$

The minimum impact parameter is the relativistic deBroglie wavelength of the β -particle given by $\lambda_e = hc/(\gamma E_r \beta)$. On scales $\lesssim \lambda_e$, β -particles cannot be localized due to the Heisenberg uncertainty principle. The maximum impact parameter is the Debye length of the ejecta (Eq. 13).

To leading order in $1 - \mu_{\text{cm}}$, the integrated cross section is

$$\sigma_{\text{mol}}(\mu_{\text{s,cm}}) = 2 \int_0^{\mu_{\text{s,cm}}} d\mu'_{\text{cm}} \frac{d\sigma_{\text{mol}}}{d\mu'_{\text{cm}}} \approx 8\pi \left(\frac{r_0}{\gamma\beta} \right)^2 \frac{\gamma + 1}{\beta^2} \frac{1}{1 - \mu_{\text{s,cm}}}. \quad (22)$$

Similar to our calculation of Mott scattering (Sec 2.3.5), the scattering angle and impact parameter are related by $1 - \mu_{\text{s,cm}} \propto b^{-2}$. Computing the stopping cross section (Eq. 5) for the Møller differential cross section (Eq. 18) and energy loss (Eq. 21) to leading order in $1 - \mu_{\text{s,cm}}$ gives

$$S_{\text{mol}} \approx 8\pi \left(\frac{r_0}{\gamma\beta} \right)^2 \frac{\gamma + 1}{\beta^2} \ln \Lambda' \cdot E \approx 2.0 \times 10^{-20} (\gamma + 1) \gamma^{-2} \beta^{-4} \ln \Lambda' \text{ cm}^2 \cdot E, \quad (23)$$

where $\ln \Lambda' = \ln(\lambda_D/\lambda_e) = \ln \Lambda + \ln(\gamma\beta)$ and $\ln \Lambda$ is given by Equation 15. Computing the transport cross section (Eq. 5) for the Møller differential cross section and fluid frame scattering angle (Eq. 20) to leading order in $1 - \mu_{\text{s,cm}}$ gives

$$\sigma_{\text{t,mol}} \approx 8\pi \left(\frac{r_0}{\gamma\beta^2} \right)^2 \ln \Lambda' \approx 2.0 \times 10^{-20} \gamma^{-2} \beta^{-4} \ln \Lambda' \text{ cm}^2, \quad (24)$$

which only differs from the stopping cross section by a factor $(\gamma + 1)E$.

2.5 Total stopping and transport cross sections

In Figure 5, we show the stopping and transport cross sections for Helium ($Z = 2$), Iron ($Z = 26$), Tellurium ($Z = 52$), and Uranium ($Z = 92$) targets as a function of electron energy and ionization stage. The stopping cross section is partitioned into contributions from EII, EIE, and bremsstrahlung.

Energy loss is driven by EII at MeV energies, but EIE dominates at lower energies $\lesssim 1$ keV. At the first ionization threshold, the EII contribution rises sharply, while the EIE contribution is negligible until somewhat higher energies where strong dipole-allowed excitation channels become available. Bremsstrahlung does not contribute significantly to the stopping cross section at MeV energies, although it dominates at GeV energies beyond the limit of the plot. Heavier species have higher stopping cross sections and greater relative contributions from EIE and bremsstrahlung.

At low energies $\lesssim 1$ keV, the transport cross section is dominated by the small-angle Mott contribution, so it scales as E^{-2} and is sensitive to the target ionization stage. At higher energies, the transport cross section is augmented by the large-angle Mott contribution, so it is insensitive to the target ionization stage and increases for heavier species.

If we let x_{iq} denote the number fraction of element in ionization stage q , then the total stopping and transport cross sections can be expressed as an abundance-weighted sum over the contributions from each species according to

$$S_{\text{tot}} = \mu_{\text{mmw}} \sum_i Y_i \sum_q x_{iq} S_{iq} + \bar{q} S_e \quad (25)$$

$$\sigma_{\text{t,tot}} = \mu_{\text{mmw}} \sum_i Y_i \sum_q x_{iq} \sigma_{\text{t},iq} + \bar{q} \sigma_{\text{t},e}, \quad (26)$$

where S_{iq} and $\sigma_{\text{t},iq}$ are the stopping and transport cross sections for species (i, q) , and S_e and $\sigma_{\text{t},e}$ are the electron stopping and transport cross sections due to Møller scattering. These quantities are related to the mass stopping power and transport opacity by

$$-\frac{1}{\rho} \frac{dE}{dx} = \frac{N_A}{\mu_{\text{mmw}}} S_{\text{tot}}, \quad \kappa_{\text{t}} = \frac{N_A}{\mu_{\text{mmw}}} \sigma_{\text{t,tot}}. \quad (27)$$

In Figure 6, we plot the total mass stopping power and transport opacity as a function of electron energy for our strong r -process abundance at 30 days post-merger. The results are similar to the results for individual elements (Fig. 5), except for the contributions from Møller scattering. These contributions dominate at low energies $\lesssim 1$ keV and become stronger at higher ionization stages, suggesting that low energy β -particles rapidly thermalize due to Coulomb interactions with thermal electrons.

2.6 Ionization cascade

EII generates a population of secondary electrons with a wide energy distribution that peaks at ~ 100 eV and has a long tail at higher energies. As the secondary population thermalizes, it produces a population of tertiary electrons. Iterating this process results in an ionization cascade. In this section, we calculate the effect of the ionization cascade on the overall ionization rate.

As an electron of energy E thermalizes, the number of times it ionizes a species (i, q) is

$$N_{\text{ion},iq}(E) = \int dt \frac{\Gamma_{\text{ion},iq}}{dE/dt} = Y_i x_{iq} \mu_{\text{mmw}} \int_0^E dE' \frac{\sigma_{\text{EII},iq}(E')}{S_{\text{tot}}(E')}, \quad (28)$$

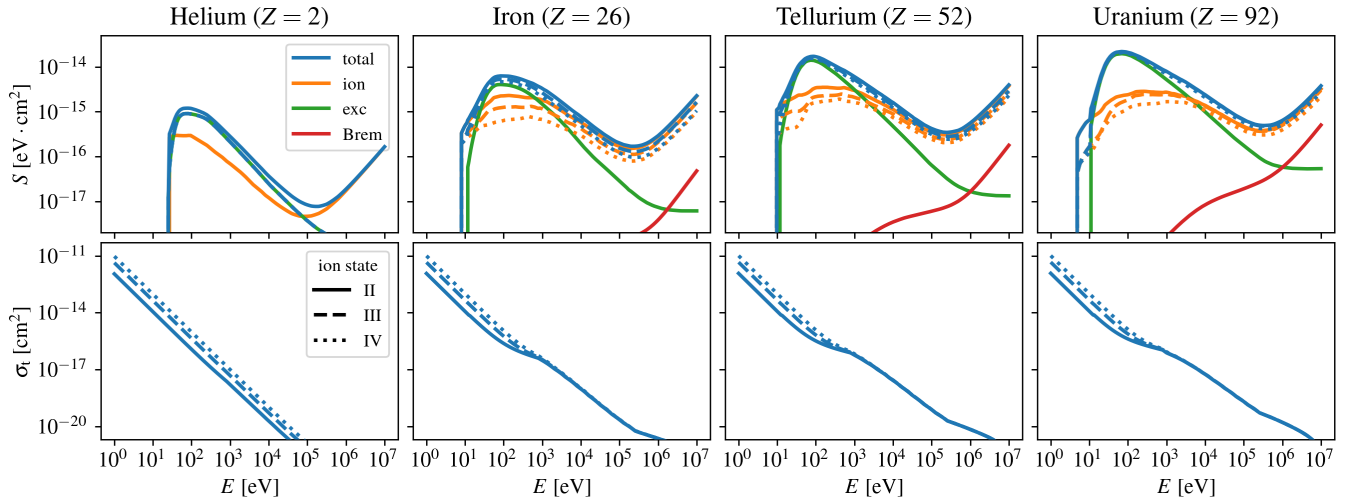


Figure 5. stopping cross section (top row) and transport cross section (bottom row) for Helium ($Z = 2$) (first column), Iron ($Z = 26$) (second column), Tellurium ($Z = 52$) (third column), and Uranium ($Z = 92$) (fourth column) as a function of electron energy. The stopping cross section is partitioned into contributions from EII (orange), EIE (green), and bremsstrahlung (red). Each target ionization stage is shown in a different linestyle indicated by the legend. Energy loss is driven by EII at MeV energies, but EIE dominates at lower energies $\lesssim 1$ keV. Bremsstrahlung does not contribute significantly to the stopping cross section at MeV energies, although it dominates at GeV energies beyond the limit of the plot. At low energies $\lesssim 1$ keV, the transport cross section is dominated by the small-angle Mott contribution, so it scales as E^{-2} and is sensitive to the target ionization stage. At higher energies, the transport cross section is augmented by the large-angle Mott contribution, so it is insensitive to the target ionization stage. Heavier species have higher transport cross sections, higher stopping cross sections, and greater relative contributions from EIE and bremsstrahlung.

where $\Gamma_{\text{ion},iq} = n_{iq}v\sigma_{\text{EII},iq}$ is the ionization rate of species (i, q) . Similarly, as an electron at energy E thermalizes, the spectrum of secondaries it produces at energy E' is

$$\left. \frac{dN_{\text{sec}}(E)}{dE'} \right|_{E'} = \int_0^E \frac{dE''}{S(E'')} \frac{d\sigma_{\text{sec}}(E'')}{dE'}, \quad (29)$$

where $d\sigma_{\text{sec}}(E)/dE'$ is the differential cross section for an electron at energy E to produce a secondary electron at energy E' , including contributions from all target species.

Convolving the number of ionizations with the differential cross section for secondaries, we get the effective ionization cross section due to secondaries,

$$\sigma_{\text{ion},iq}(E) = \int dE' N_{\text{ion},iq}(E') \frac{d\sigma_{\text{sec}}(E)}{dE'}. \quad (30)$$

Similarly, convolving the secondary spectrum with the differential cross section for secondaries, we get the differential cross section for tertiaries,

$$\frac{d\sigma_{\text{ter}}(E)}{dE'} = \int dE'' \frac{dN_{\text{sec}}(E'')}{dE''} \frac{d\sigma_{\text{sec}}(E)}{dE''}. \quad (31)$$

These calculations can be iterated for successive generations by substituting the result of Equation 31 for $d\sigma_{\text{sec}}(E)/dE'$ in Equations 30 and 31. In Figure 7, we show the EII cross section for different incident electron energies partitioned into contributions from each generation of the ionization cascade. The cascade (secondaries and beyond) contributes significantly to the EII cross section across all elements, similar to the conclusion reached by [Van den Berg & Hotokezaka \(2026\)](#) using the Spencer-Fano formalism. The cascade contribution increases with incident electron energy, becoming similar to the primary contribution at 1 MeV.

2.7 Other sources of supra-thermal electrons

When ionization leaves an atom with an inner-shell vacancy, the atom may undergo Auger-Meitner ionization, in which a higher-energy electron fills the vacancy and the liberated energy goes into unbinding a different electron in the same atom. However, these electrons are much less abundant than the secondary population discussed above because the inner shells only contribute a small fraction to the EII cross section and not every inner shell vacancy produces an Auger-Meitner electron, so we neglect their contribution to the ionization rate. This assumption is verified by [Van den Berg & Hotokezaka \(2026\)](#), who show that Auger-Meitner electrons contribute $\lesssim 10\%$ to the steady-state electron spectrum.

Auger-Meitner electrons can also be produced in some β decays where the daughter nucleus has an inner-shell vacancy (they are also known as internal conversion electrons in this context). Using data from Oleg Korobkin (private communication), we compute the β decay spectrum accounting for this population. However, we found that they had a negligible impact on the decay spectrum, so we do not include their contribution in our analysis.

Supra-thermal electrons can also be produced by γ -rays through Compton scattering of free thermal electrons and photoionization of bound electrons. However, the ejecta become transparent to γ -rays only a few days post-merger ([Barnes et al. 2016](#)), so we neglect their contribution.

2.8 Other interactions

2.8.1 Synchrotron losses

The gyro-oscillations of an electron in a magnetic field with amplitude B produce synchrotron radiation at a power given by

$$P_{\text{sync}} = \frac{2}{3} \frac{e^4 B^2}{m_e^2 c^3} \gamma^2 \beta^2 (1 - \mu^2), \quad (32)$$

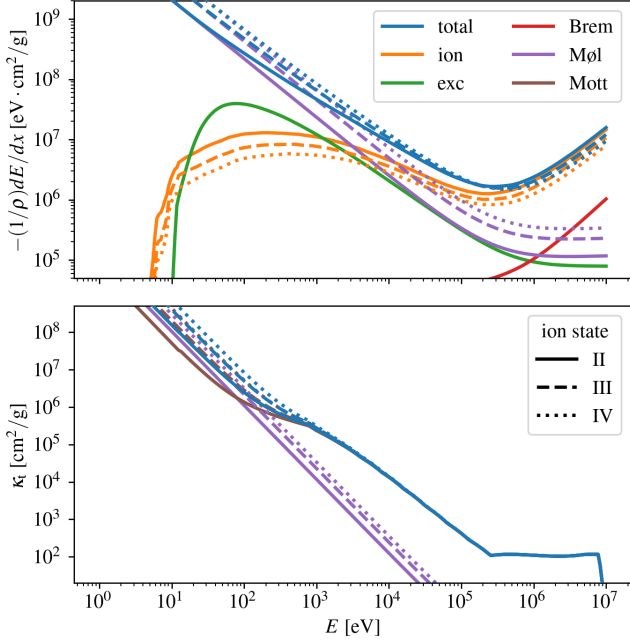


Figure 6. Mass stopping power (top panel) and transport opacity (bottom row) as a function of electron energy for our strong r -process abundance at 30 days post-merger. The mass stopping power is partitioned into contributions from EII (orange), EIE (green), bremsstrahlung (red), and Møller scattering (purple). The transport opacity is partitioned into contributions from Mott scattering (brown) and Møller scattering (purple). Each target ionization stage is shown in a different linestyle indicated by the legend. The results are similar to the results for individual elements (Fig. 5), except for the contributions from Møller scattering. These contributions dominate at low energies $\lesssim 1$ keV and become stronger at higher ionization stages. Low energy β -particles rapidly thermalize due to Coulomb interactions with thermal electrons.

where B is the magnetic field amplitude and μ is the cosine of the pitch angle between the particle velocity and magnetic field direction. For a 1 MeV electron in a 10^{-6} G field, the synchrotron mass stopping power is $\sim 10^{-4}$ eV cm²/g, which is insignificant compared to other energy loss mechanisms, so we neglect synchrotron losses, similar to Barnes et al. (2016).

2.8.2 Cherenkov radiation

In a plasma, electrons with velocities faster than the phase velocity v_φ excite electrostatic plasma oscillations along their trajectories, creating an electromagnetic wakefield analogous to the Cherenkov effect in optics (Cohen 1961). An unmagnetized plasma can be modeled as a dispersive medium with relative dielectric constant $1 - (\omega_p/\omega)^2$, where ω_p is the plasma frequency, given by $\omega_p = \sqrt{4\pi n_e e^2/m_e}$.

By solving Maxwell’s equations for an electron moving through the plasma, one can derive the power in Cherenkov radiation. In a naïve calculation, the Cherenkov power diverges. However, in practice, Landau damping inhibits the propagation of plasma waves when their phase velocity is close to the thermal velocity of free electrons, given by $v_{\text{thm}} = \sqrt{3k_B T/(2m_e)}$.

Following Cohen (1961), we assume that the Cherenkov radiation spectrum is zero if $v_\varphi < \sqrt{2}v_{\text{thm}}$. Under this assumption, the

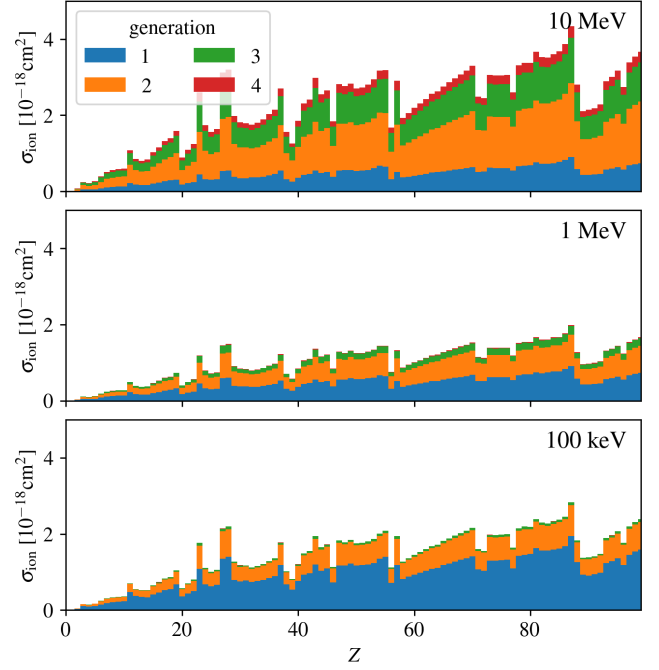


Figure 7. Per-element electron impact ionization (EII) cross sections for three incident electron energies: 10 MeV (top panel), 1 MeV (middle panel), bottom panel (100 keV). Cross sections are partitioned into contributions from each generation of the ionization cascade (Sec. 2.6): primaries (blue), secondaries (orange), tertiaries (green), and quaternaries (red). The cascade (secondaries and beyond) contributes significantly to the EII cross section across all elements. The cascade contribution increases with incident electron energy, becoming similar to the primary contribution at 1 MeV.

Cherenkov power is given by

$$P_{\text{cher}} = \frac{e^2 \omega_p^2}{2v^2} \ln \left[\left(\frac{v}{v_{\text{thm}}} \right)^2 - 1 \right]. \quad (33)$$

For a 1 MeV electron in a singly ionized plasma at temperature 10^3 K, density 10^{-14} g/cm³, and mean molecular weight 140, the Cherenkov mass stopping power is ~ 5 eV cm²/g, which is insignificant compared to other energy loss mechanisms, so we do not include Cherenkov losses in our model. The Cherenkov stopping power increases for lower energy electrons, but nevertheless is always a small fraction of the Møller stopping power.

In a magnetized plasma, additional modes can be excited, such as Whistler and ion cyclotron waves (McKenzie 1967). These effects have been explored by previous work in the context of pulsed electron beams in the Earth’s magnetosphere (Harker & Banks 1984; Farrell & Goertz 1990; Delzanno & Roytershteyn 2019). However, given the weak magnetic fields in our application and our initial estimate for the mass stopping power, we leave the task of generalizing these models to individual electrons to future work.

2.9 Public data

We make the per-species stopping, transport, and EII cross sections available online.⁴ We also provide combined cross sections using our strong r -process abundance pattern at 30 days post-merger. For

⁴ zandalman.com/publications/Andalman+2026b/

the stopping and transport cross sections, we separately tabulate the Mott and Møller contributions proportional to $\ln \Lambda$ and \bar{q}^2 , allowing the data to be adapted to arbitrary values of these quantities. For the EII cross sections, we provide values including and excluding the contribution from the ionization cascade.

3 GLOBAL MODEL

3.1 Toy model

The dynamical ejecta are expected to have masses in the range $10^{-4} - 10^{-2} M_{\odot}$, velocities in the range $0.1 - 0.3c$, and electron fractions in the range $0.05 - 0.4$ based on theoretical work (Rosswog et al. 1999; Rosswog 2013; Bauswein et al. 2013; Hotokezaka et al. 2013; Wanajo et al. 2014; Kyutoku et al. 2015; Sekiguchi et al. 2016; Radice et al. 2018). The mass and velocity ranges are broadly consistent with modeling of AT2017gfo (Smartt et al. 2017; Kasliwal et al. 2017; Abbott et al. 2017b; Cowperthwaite et al. 2017; Rosswog et al. 2018).

After the merger, the ejecta expands rapidly. As the flow becomes supersonic, the expansion becomes approximately homologous. This behavior arises naturally in simulations (Rosswog et al. 2014; Grossman et al. 2014) and is often assumed in light-curve calculations (Metzger et al. 2010; Kasen et al. 2017; Tanaka et al. 2017; Bulla 2019; Kawaguchi et al. 2020; Korobkin et al. 2021), yielding similar results to full radiation-hydrodynamic calculations (Wu et al. 2022).

In the homologous model, at time t post-merger, the ejecta extends out to a radius

$$R_{\text{ej}} = v_{\text{ej}} t \simeq 5.2 \times 10^{14} v_{0.2} t_{\text{d}} \text{ cm}, \quad (34)$$

where $v_{0.2} \equiv v_{\text{ej}}/0.2c$ and t_{d} is the time in days. The average density of the ejecta is

$$\bar{\rho} = (3/4)\pi^{-1} M_{\text{ej}} R_{\text{ej}}^{-3} \simeq 3.4 \times 10^{-14} M_{0.01} v_{0.2}^{-3} t_{\text{d}}^{-3} \text{ g/cm}^3, \quad (35)$$

where $M_{0.01} \equiv M_{\text{ej}}/10^{-2} M_{\odot}$.

We assume that the ejecta mass is distributed in velocity space according to a power law given by $dM/du \propto u^{2-\alpha}$, where u is the ejecta velocity and $\alpha \sim 0.5 - 3.0$ (Bauswein et al. 2013; Metzger 2019; Fryer et al. 2024). Under homologous expansion, $u \propto r$, so this approach is equivalent to a radial density profile $\rho \propto r^{-\alpha}$.

Modeling of AT 2017gfo suggests that the effective temperature scales as $t^{-\beta}$, where $\beta \sim 0.5 - 0.8$, reaching $300 - 10^4$ K at late times (Drout et al. 2017; Waxman et al. 2018; Sneppen et al. 2024; Fryer et al. 2024). However, radiative transfer simulations show the gas temperature does not follow this scaling, and instead increases at late times (Pognan et al. 2022a; Brethauer et al. 2026). The temperature only affects the microphysics weakly through the Coulomb logarithm (Sec. 2), so we adopt a nominal value of 10^3 K.

If the magnetic flux is frozen into the ejecta, then the field strength is (Barnes et al. 2016)

$$\bar{B} = B_0 (R_0/R_{\text{ej}})^2 \simeq 3.7 B_{12} R_6^2 v_{0.2}^{-2} t_{\text{d}}^{-2} \mu\text{G}, \quad (36)$$

where B_0 and R_0 are the magnetic field strength and radius at the time of mass ejection, $B_{12} \equiv B_0/10^{12}$ G and $R_6 \equiv R_0/10^6$ cm. B_0 ranges from 10^9 to 10^{15} G depending on the initial NS magnetic fields and the efficiency of magnetic field amplification (Price & Rosswog 2006; Kiuchi et al. 2015, 2018). R_0 can be interpreted as the characteristic size of the neutron stars or the post-merger accretion disk, which ranges from 10^6 to 10^7 cm.

In a magnetic field, the motion of charged particles is affected by the Lorentz force. For a constant or slowly-varying field, particle trajectories are described by circular motion about a guiding center

that moves parallel to the field. These gyro-oscillations have radius $r_g = \gamma m_e v (1 - \mu^2)/(eB)$, where μ is the cosine pitch angle between the velocity and magnetic field. In the non-relativistic (NR) and ultra-relativistic (UR) limits, the gyro-to-ejecta radius ratio is

$$r_g/R_{\text{ej}} \simeq 1.7 \times 10^{-6} B_{12}^{-1} R_6^{-2} v_{0.2} t_{\text{d}} \begin{cases} E_{\text{MeV}}^{1/2} & \text{NR} \\ E_{\text{MeV}} & \text{UR}, \end{cases} \quad (37)$$

where $E_{\text{MeV}} = E/\text{MeV}$. For most realistic parameters, β -particles are well-magnetized and are transported parallel to the magnetic field. This behavior makes the thermalization efficiency sensitive to the magnetic field geometry (Barnes et al. 2016).

If magnetic fields are radial, then charged particles stream out of the ejecta and deposit less energy. If magnetic fields are toroidal or highly turbulent, then charged particles may be trapped in the ejecta. These effects have been previously discussed in the context of positron emission from core collapse supernovae (Colgate et al. 1980; Chan & Lingefelter 1993; Milne et al. 1999), motivated by the need to explain the strength of the Galactic gamma-ray emission line at 511 keV produced by positron annihilation (Siebert 2023). In these systems, radio (Dickel & Milne 1976; Milne 1987; Dubner & Giacani 2015) and X-ray polarimetry (Vink et al. 2022) favor radial magnetic fields in young supernova remnants, with an increasing turbulent component as the remnants age. While the physical conditions in KNe differ, these observations motivate considering a variety of magnetic field morphologies in the ejecta.

3.2 Transport equations

We use Monte Carlo simulations to model β -particle transport and thermalization in the ejecta. We model the ejecta as a spherically symmetric, homologously expanding flow, which reduces the problem to one spatial dimension in radius. It is convenient to work in velocity coordinates $u = r/t$, which are constant along a Lagrangian position in the ejecta. We define two reference frames: the lab frame, the rest frame of the ejecta center-of-mass; and the local comoving frame (LCF), the rest frame of the fluid at the location of a β -particle. We denote LCF quantities with primes and lab-frame quantities without primes.

Electron transport in tangled magnetic fields is a complex process involving guiding center drifts, wave-particle interactions, and resonant scattering (for a review, see Verscharen et al. 2026). Given the uncertainty in the magnetic field structure, we consider two limiting cases for transport rather than modeling electron transport in detail: particles moving through coherent radial magnetic fields and particles that are completely trapped.

Radial fields maximize particle transport because particles stream along radial field lines and are accelerated by magnetic focusing. For this scenario, we show that the 1D transport equations are mathematically equivalent to a scenario with no magnetic field.

The completely trapped limit could arise in toroidal magnetic fields that trap particles at a single velocity coordinate, or in highly tangled magnetic fields that trap particles in small-scale magnetic structures. For more realistic field geometries, like the ‘‘random field’’ model considered by Barnes et al. (2016), particle transport is expected to produce results in-between these two extremes. Magnetized turbulence may also modify the electron spectrum through particle acceleration processes such as diffusive shock acceleration, but these effects are beyond the scope of this work.

It is convenient to work with dimensionless components of the particle 4-momentum: the particle Lorentz factor γ and the dimensionless momenta $p_{\parallel} = \gamma v \mu$ and $p_{\perp} = \gamma v (1 - \mu^2)^{1/2}$, where v is the

particle velocity in units of c and μ is the cosine angle between the velocity and the radial direction. They are related by

$$\gamma^2 = 1 + p_{\parallel}^2 + p_{\perp}^2 \quad (38)$$

and their values between reference frames are related by a Lorentz transformation, i.e.

$$\gamma = \gamma_u(\gamma' + up'_{\parallel}) \quad \gamma' = \gamma_u(\gamma - up_{\parallel}) \quad (39)$$

$$p_{\parallel} = \gamma_u(p'_{\parallel} + u\gamma') \quad p'_{\parallel} = \gamma_u(p_{\parallel} - u\gamma) \quad (40)$$

$$p_{\perp} = p'_{\perp}, \quad (41)$$

where $u = r/t$ is the fluid velocity in units of c and $\gamma_u = (1 - u^2)^{-1/2}$ is the fluid Lorentz factor. Time between reference frames is related by the Doppler factor given by

$$D \equiv \frac{dt}{dt'} = \frac{\gamma}{\gamma'} = \gamma_u \frac{\gamma' + up'_{\parallel}}{\gamma'}. \quad (42)$$

As the particle travels, it experiences a velocity gradient given by

$$\frac{du}{dt'} = D \frac{\mu v - u}{t} = D \frac{p_{\parallel} - u\gamma}{\gamma t} = \frac{p'_{\parallel}}{\gamma_u \gamma' t}. \quad (43)$$

As a result, the energy and momentum in the LCF evolve, even in the absence of collisional losses. In the absence of a magnetic field, particles stream freely and the parallel momentum evolves due to the rotation of the radial unit vector along straight-line trajectories

$$\left. \frac{dp_{\parallel}}{dt'} \right|_{\text{geo}} = D \frac{d\hat{\mathbf{r}}}{dt} \cdot \mathbf{p} = D \frac{p'_{\perp}}{\gamma u t} = \frac{p'_{\perp}}{\gamma' u t}. \quad (44)$$

In a coherent radial magnetic field frozen into the ejecta, flux conservation implies $B \propto r^{-2}$. Assuming that the electrons are well-magnetized, the resulting field gradient produces a lab-frame mirror force (Kulsrud 2005)

$$\left. \frac{dp_{\parallel}}{dt'} \right|_{\text{mir}} = -D \mu_{\text{mag}} \frac{dB}{dr} = D \frac{p'_{\perp}}{\gamma u t} = \frac{p'_{\perp}}{\gamma' u t}, \quad (45)$$

where $\mu_{\text{mag}} = p_{\perp}^2 / (2\gamma B)$ is the magnetic moment. This result is the same as Equation 44, so this scenario is mathematically equivalent to the free-streaming case. In this configuration, the magnetic field and the fluid velocity are parallel, so there is no motional electric field and thus no lab-frame energy evolution.

Differentiating Equations 39 and 40 with respect to LCF time, we find

$$\frac{d\gamma'}{dt'} = \gamma_u \frac{d\gamma}{dt'} - u\gamma_u \frac{dp_{\parallel}}{dt'} - \gamma_u^2 p'_{\parallel} \frac{du}{dt'} \quad (46)$$

$$\frac{dp'_{\parallel}}{dt'} = \gamma_u \frac{dp_{\parallel}}{dt'} - u\gamma_u \frac{d\gamma}{dt'} - \gamma_u^2 \gamma' \frac{du}{dt'}. \quad (47)$$

Setting the change in lab-frame energy to zero and substituting our expressions for the change in the velocity coordinate (Eq. 43) and parallel momentum (Eq. 44), we find

$$\left. \frac{d\gamma'}{dt'} \right|_{\text{ad}} = -\gamma_u \frac{\gamma'^2 - 1}{\gamma' t} \quad (48)$$

$$\left. \frac{dp'_{\parallel}}{dt'} \right|_{\text{ad}} = \gamma_u \frac{p'_{\perp}{}^2 - u\gamma' p'_{\parallel}}{\gamma' u t}. \quad (49)$$

In terms of kinetic energy, Equation 48 is

$$\left. \frac{\partial E'}{\partial t'} \right|_{\text{ad}} = -\gamma_u v'^2 \frac{E' + E_{\tau}}{t}, \quad (50)$$

which we can verify by taking appropriate limits. For a non-relativistic fluid, we have $u \ll 1$. In the non-relativistic particle limit

$v \ll 1$, and we have $d_{\tau} E' |_{\text{ad}} = -v'^2/t = -2E'/t$, which gives the standard result $E' |_{\text{ad}} \propto t^{-2} \propto \rho^{2/3}$. In the ultra-relativistic particle limit $v \approx 1$, and we have $d_{\tau} E' |_{\text{ad}} = -E'/t$, which gives the standard result $E' |_{\text{ad}} \propto t^{-1} \propto \rho^{1/3}$.

The LCF energy also evolves due to collisional losses $d_{\tau} \gamma' |_{\text{coll}}$. Collisional losses preserve direction, so the parallel momentum also evolves to maintain a constant ratio of $p'_{\perp}/p'_{\parallel}$. Fixing $p'_{\perp}/p'_{\parallel}$ and differentiating Equation 38, we find

$$\left. \frac{dp'_{\perp}}{dt'} \right|_{\text{coll}} = \frac{\gamma' p'_{\perp}}{\gamma'^2 - 1} \left. \frac{d\gamma'}{dt'} \right|_{\text{coll}}. \quad (51)$$

Combining adiabatic and collisional terms, the evolution equations are

$$\frac{d\gamma'}{dt'} = \left. \frac{d\gamma'}{dt'} \right|_{\text{coll}} - \gamma_u \frac{\gamma'^2 - 1}{\gamma' t} \quad (52)$$

$$\frac{dp'_{\parallel}}{dt'} = \frac{\gamma' p'_{\parallel}}{\gamma'^2 - 1} \left. \frac{d\gamma'}{dt'} \right|_{\text{coll}} + \gamma_u \frac{p'_{\perp}{}^2 - u\gamma' p'_{\parallel}}{\gamma' u t}. \quad (53)$$

In the trapped limit, we assume the velocity coordinate does not evolve, so $du/dt = 0$. In this case, the adiabatic energy loss term is the standard result for an isotropic gas, which is equivalent to Equation 48, so the resulting energy evolution equation is equivalent to Equation 52.

3.3 Monte Carlo methods

We model β -particles as discrete packets of equal energy in the LCF with state variables of time, velocity coordinate, LCF energy, and LCF parallel momentum. For the radial field scenario, the evolution equations are Equations 43, 52, and 53. For the trapped scenario, u does not evolve and the system is independent of p_{\parallel} .

We assume that the ejecta has a power-law density profile $\rho = C_{\rho} u^{-\alpha} t^{-3}$, where $C_{\rho} = (3 - q)/(4\pi) M_{\text{ej}} v_{\text{ej}}^{-(3-\alpha)}$ is a normalization constant. To spawn the packets, we sample the initial time from the energy injection rate $t \sim \partial_{\tau} \varepsilon(t)$, the initial velocity coordinate from the ejecta mass profile $u \sim (1/u^2) \partial_u \rho(u)$, the initial LCF energy from the decay energy spectrum $E' \sim E' \partial_{E'} \Gamma_{\text{dec}}(t, E')$, and the initial LCF cosine angle from an isotropic distribution $\mu' \sim \mathcal{U}$. The Lorentz factor and parallel momentum are then $\gamma' = 1 + E'/E_{\tau}$ and $p'_{\parallel} = \mu' \sqrt{\gamma'^2 - 1}$.

We sample the energy injection rate numerically by using the cumulative trapezoid method to calculate the CDF and invert it with linear interpolation. We cut off the injection rate at early times < 1 day when most particles thermalize locally and late times > 1 yr when most particles escape. The late-time cutoff only misses 4% of the decay energy after 1 day. Using the initial time, we select a decay energy spectrum from a pre-tabulated grid of times and sample the initial LCF energy numerically. We sample the velocity coordinate and cosine angle direction using the analytic inverse CDFs of their respective distributions: $u = \xi^{1/(3-q)} v_{\text{ej}}$ and $\mu' = 2\xi - 1$.

The mean free path of a packet is given by the energy-dependent transport opacity $\lambda_{\text{mfp}} = 1/(\rho \kappa_{\tau})$. We assume that a packet scatters isotropically in the LCF after reaching an optical depth sampled from an exponential distribution $\tau_* = -\ln \xi$, where the optical depth is defined by $d\tau = \kappa_{\tau} \rho' v' dt'$. Within each Monte Carlo step, we integrate lab-frame time, velocity coordinate, energy, and parallel momentum as a function of optical depth by multiplying their derivatives with respect to LCF time by $d_{\tau} t'$.

We set the integration step $\Delta\tau$ to the minimum of $\tau_* - \tau$, $f \cdot f \cdot E' / d_{\tau} E'$, and $f \cdot R_{\text{ej}} / (v' d_{\tau} t')$, where we use $f = 0.01$. This choice ensures that we never overshoot τ_* and that changes in optical depth,

energy, and velocity coordinate are well sampled. At each integration step, we compute the velocity coordinate and LCF energy, and we select the stopping power, transport opacity, and ionization rate from a pre-tabulated grid of energies.

If τ reaches τ_* , we model isotropic scattering by resampling the LCF cosine angle from a uniform distribution. However, if an end condition is reached, we terminate the packet evolution. The end conditions are (i) $E < E_{\text{thm}} = 1$ eV, complete thermalization; (ii) $u > v_{\text{ej}}$, escape; and (iii) $t > t_{\text{max}} = 1$ yr, persistence. We assume that persistent packets eventually escape with negligible additional thermalization because the ejecta becomes very diffuse at late times.

Each packet represents an LCF energy $E'_{\text{tot}}/N_{\text{pac}}$ or, equivalently, a number of packets $E'_{\text{tot}}/(E_i N_{\text{pac}})$, where $E'_{\text{tot}} = M_{\text{ej}} \int dt \partial_t Q_{\text{inj}}$ is the total injected LCF energy, N_{pac} is the total number of packets, and E'_i is the LCF energy of the packet at injection. As the simulation runs, we keep track of energy deposition and ionizations on a 128^2 grid in logarithmic time and velocity coordinate.

We neglect the effect of changes in the elemental abundances over time, which has a negligible effect on the stopping power and transport opacity, instead fixing the elemental abundances to their value at 30 days post-merger. Similarly, we neglect the effect of changes in the Coulomb logarithm over time (Eq. 15), instead setting it using our nominal temperature of 10^3 K and the average ejecta density at 30 days post-merger.

We implement these Monte Carlo simulations in a PYTHON script, parallelized with MPI4PY (Dalcín et al. 2005) and accelerated by NUMBA (Lam et al. 2015) using just-in-time compilation. We run simulations over a variety of ejecta models, parameterized by ejecta mass, velocity, r -process model, ionization state, and density profile power-law exponent. For our fiducial ejecta model, we use a strong r -process with singly ionized ejecta, $M_{\text{ej}} = 0.003 M_{\odot}$, $v_{\text{ej}} = 0.2c$, and $\alpha = 1$. For each transport limit, we run a grid of ejecta mass, velocity, and density power-law slope $\{0.001, 0.003, 0.01, 0.03\} M_{\odot} \times \{0.1, 0.2, 0.3\} c \times \{1.0, 2.0\}$ and a grid of r -process models and ionization states $\{\text{weak, medium, strong}\} \times \{\text{II, III, IV}\}$, making 56 simulations in total. Each model was run on eight 2.9 GHz Intel Cascade Lake processors for 12 hours, resulting in roughly 50 million packets.

4 RESULTS

4.1 Particle trajectories

The expansion of the ejecta has multiple effects on β -particle thermalization. As the stopping power decreases, particles persist longer in the ejecta, so thermalization becomes increasingly non-local in space and time, and particles lose more energy to adiabatic expansion. Simultaneously, as the transport cross section decreases, scattering becomes less frequent and particles are more likely to escape before completely thermalizing. In Figure 8, we showcase these effects in our fiducial ejecta model for a radial magnetic field by injecting 1-MeV particles by-hand at times 1, 3, 9, 27, 81, and 243 days and velocity coordinates $0.05c$ and $0.15c$.

Initially, particles thermalize locally in space and time. Later on, particles persist in the ejecta and thermalization becomes non-local. As typical distance particles are transported before thermalizing increases, transport becomes increasingly biased towards larger velocity coordinates due to magnetic mirroring and focusing, or due to geometry in the equivalent unmagnetized scenario.

Some particles escape before they completely thermalize, while others are trapped by scattering, especially those injected at small velocity coordinate where the density is higher. Initially, particle

motion can be treated as a diffusive process with coefficient $D \simeq (1/3)v\lambda_{\text{mfp}}$, where v is the particle velocity and $\lambda_{\text{mfp}} = 1/(\kappa_t\rho) \propto M_{\text{ej}}^{-1}v_{\text{ej}}^3 t^3$ is the particle mean free path. In this limit, the typical escape time is $t_{\text{esc}} \sim R_{\text{ej}}^2/D \propto M_{\text{ej}}v_{\text{ej}}^{-1}t^{-1}$.

At late times, scattering becomes inefficient and particles escape before most of their energy thermalizes. Particle motion can be treated as free-streaming when $\lambda_{\text{mfp}} \gtrsim R_{\text{ej}}$, which occurs at time $t_{\text{free}} \propto M_{\text{ej}}^{1/2}v_{\text{ej}}^{-1}$. In this limit, the typical escape time is $t_{\text{esc}} \sim R_{\text{ej}}/v \propto v_{\text{ej}}t$, which has the same time dependence as the timescale for adiabatic losses $t_{\text{ad}} = E/\dot{E}|_{\text{ad}} \propto t$. These estimates demonstrate that particle escape becomes increasingly important relative to adiabatic losses during the diffusive transport phase, but stalls relative to adiabatic losses during the free-streaming transport phase.

4.2 Thermalization efficiency and the role of transport

At each bin in time and velocity coordinate, we define the thermalization efficiency f_{thm} as the ratio of thermalized to injected energy in that bin. This definition includes thermalization contributions from particles injected at earlier times and different velocity coordinates. In Figure 9, we show the thermalization efficiency for our fiducial ejecta model in the radial field and trapped limits. We use arrows to show the average time and velocity coordinate displacement between where energy is injected and where it thermalizes.

Initially, the dense ejecta promotes local thermalization in space and time for both transport scenarios. In the trapped limit, the thermalization efficiency decreases independently at each velocity coordinate, with a more rapid decrease in the diffuse outer ejecta. In the radial field limit, particles injected at small velocity coordinates move outwards before depositing their energy, and particles injected at large velocity coordinates either escape or move inwards before depositing their energy. These effects lower the thermalization efficiency and make it more uniform across velocity coordinates in the radial field scenario.

In Figure 10, we show the thermalization efficiency integrated over velocity coordinate. We also show the injected decay energy and the energy losses due to thermalization, adiabatic losses, and escape. We plot quantities as a function of the time at which the energy is deposited or lost, and as a function of the time at which the particles carrying that energy were originally injected. At a given time, the injected energy is equal to the sum of the injection-time energy losses.

The thermalization efficiency decreases over time as the ejecta becomes more diffuse. In the trapped limit, this behavior is driven by adiabatic losses as particles persist longer in the ejecta. In the radial field limit, this behavior is mostly driven by particle escape as transport becomes more efficient, although there are still significant adiabatic losses. Energy losses due to escape initially increase faster than those due to adiabatic expansion, but follow adiabatic losses at late times. The transition occurs around 20 days, consistent with the transition from random walk to free-streaming particle trajectories in Figure 8.

During the initial phase of local thermalization, energy deposition closely tracks local injection and the deposition-time thermalization losses lie below the injection-time losses. At late times, particles persist before thermalizing, and the energy deposited at a given time becomes dominated by particles injected earlier. As a result, the deposition-time thermalization losses exceed the injection-time losses. In the trapped limit, the energy escaping at each time is identically zero because particles cannot physically escape the ejecta. However, the injection-time escape losses rise at late times as an

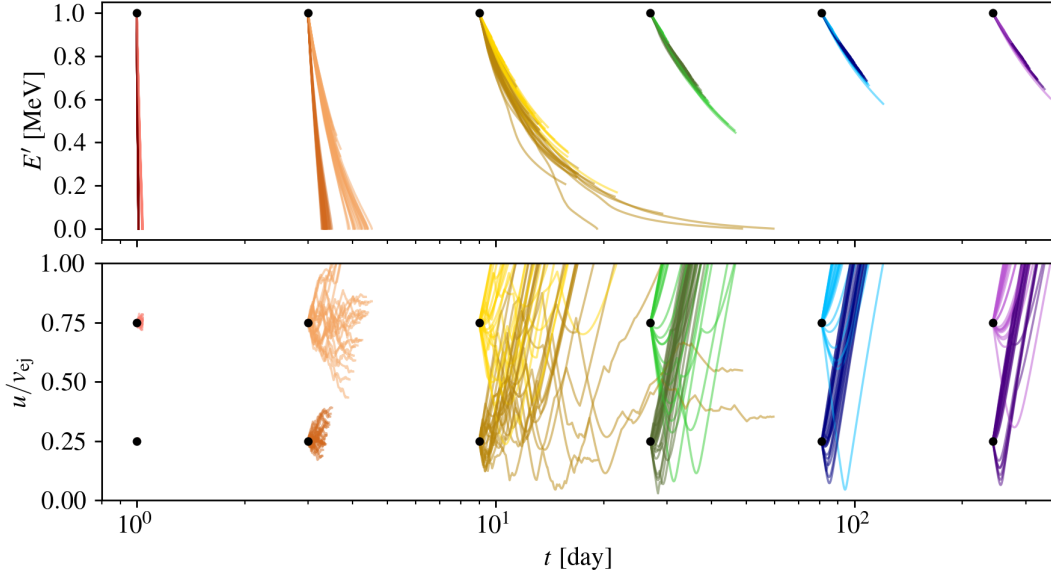


Figure 8. Velocity coordinate (bottom panel) and comoving energy (top panel) as a function of time in our fiducial ejecta model with a radial magnetic for 1-MeV particles injected by-hand at times 1 (red lines), 3 (orange lines), 9 (yellow lines), 27 (green lines), 81 (blue lines), and 243 (purple lines) days and velocity coordinates 0.05c (dark lines) and 0.15c (light lines). We inject 24 particles at each injection site (black dots). Initially, particles thermalize locally in space and time (red lines). At intermediate times, particles persist in the ejecta and thermalize non-locally in space and time (orange and yellow lines). Some particles escape before they completely thermalize, while others are trapped by scattering, especially those injected at small velocity coordinates where the density is higher. At late times, particles escape before most of their energy thermalizes (green, blue, and purple lines).

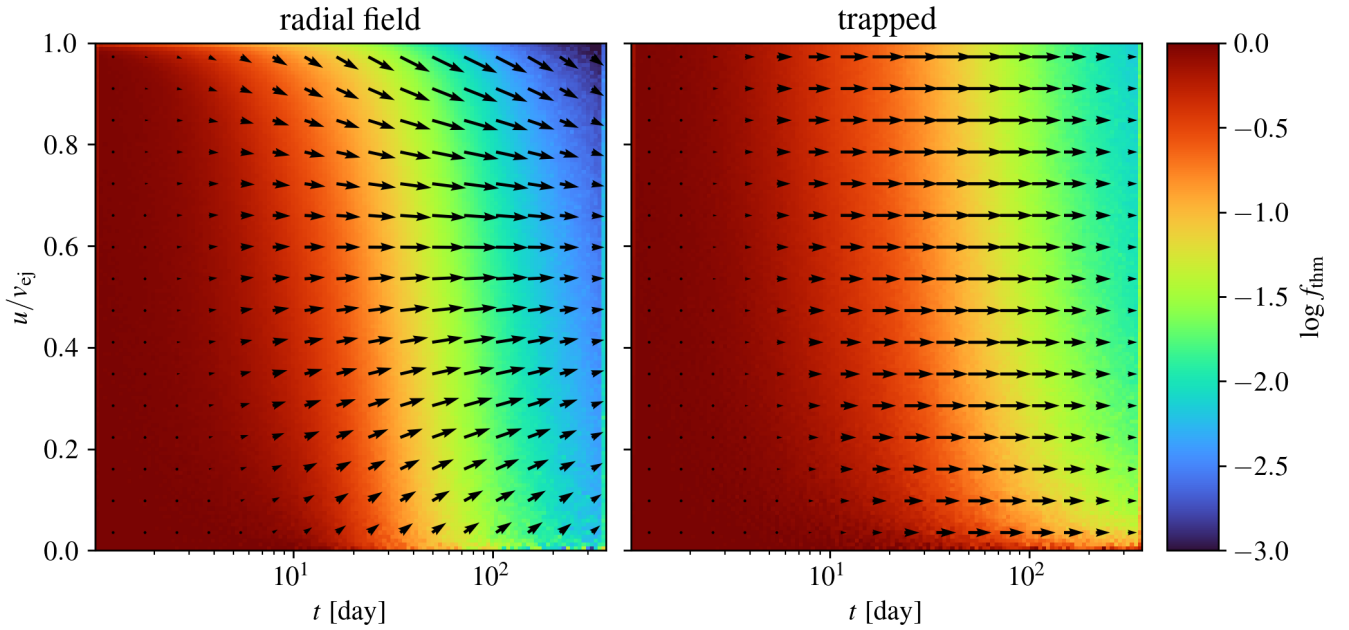


Figure 9. The thermalization efficiency at each bin in velocity coordinate and time in our fiducial ejecta model in the radial magnetic field (left panel) and trapped (right panel) limits. The arrows show the average time and velocity-coordinate displacement between where energy is injected (arrow base) and where it thermalizes. Arrow lengths are re-normalized for visual clarity. Initially, the dense ejecta promotes local thermalization in space and time for both transport scenarios. In the trapped limit, the thermalization efficiency decreases independently at each velocity coordinate, with a more rapid decrease in the diffuse outer ejecta. In the radial field limit, particles injected at small velocity coordinates move outwards before depositing their energy, and particles injected at large velocity coordinates either escape or move inwards before depositing their energy. These effects lower the thermalization efficiency and make it more uniform across velocity coordinates in the radial field scenario.

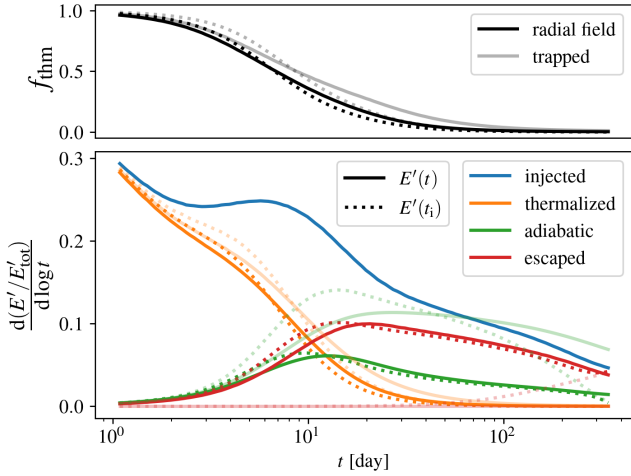


Figure 10. Thermalization efficiency (top panel), injected decay energy (bottom panel, blue lines), and energy losses (bottom panel) due to thermalization (orange lines), adiabatic losses (green lines), and escape (red lines) as a function of time in our fiducial ejecta model in the radial magnetic field (dark lines) and trapped (light lines) limits. Solid lines show quantities as a function of the time at which energy is deposited or lost, while dotted lines show quantities as a function of the time at which the particles carrying that energy were originally injected. At a given time, the injected energy is equal to the sum of the injection-time energy losses. The thermalization efficiency decreases over time as the ejecta becomes more diffuse. In the trapped limit, this decrease is driven by adiabatic losses. In the radial field limit, this decrease is mostly driven by particle escape, although there are still significant adiabatic losses.

increasing fraction of injected particles persist to the end of the simulation.

In Figure 11, we integrate the thermalization efficiency over time instead of velocity coordinate. We also show the injected decay energy and energy losses, similar to Figure 10. The energy escaping at each velocity coordinate is due to particles that persist until the end of the simulation.

The results are similar to Figure 10. The thermalization efficiency decreases with increasing velocity coordinate as the ejecta becomes more diffuse. In the trapped limit, this decrease is driven by adiabatic losses. In the radial field limit, this decrease is driven by particle escape, although there are still significant adiabatic losses. The radial field limit has lower thermalization efficiency at every velocity coordinate, with the largest differences in the innermost and outermost ejecta. At each velocity coordinate, most of the energy deposition is contributed by early times when energy deposition closely tracks local injection, so deposition-coordinate and injection-coordinate thermalization losses are nearly identical.

4.3 Inefficiency time and asymptotic slope

Motivated by the analytic arguments in Barnes et al. (2016) and Kasen & Barnes (2019), we fit our time-dependent thermalization efficiencies with an analytic form,

$$f_{\text{thm}}(t) = \frac{\ln(1 + \tau)}{\tau}, \quad \tau \equiv 2 \left(\frac{t}{t_{\text{ineff}}} \right)^{-n}, \quad (54)$$

where the inefficiency time t_{ineff} and the asymptotic slope n are free parameters. The inefficiency time represents the time after which thermalization starts to become inefficient. This formula is an *ad hoc* interpolation between limiting behaviors, with $f_{\text{thm}} \approx 1$ for $t \ll t_{\text{ineff}}$

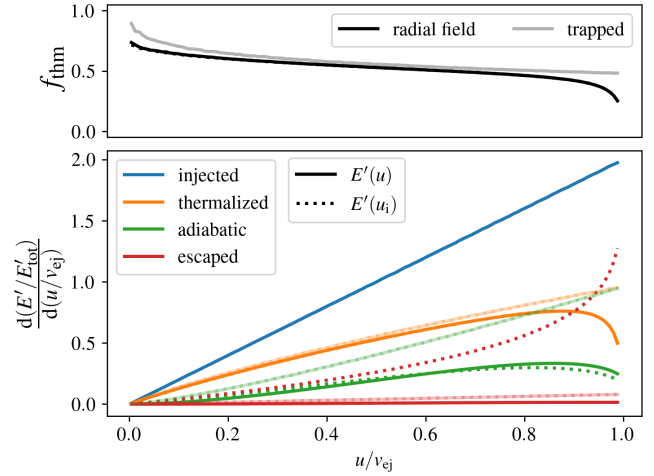


Figure 11. Same as Figure 10, but as a function of velocity coordinate instead of time. The energy escaping at each velocity coordinate is due to particles that persist until the end of the simulation (solid red lines). The injected energy increases linearly with velocity coordinate because $M \propto u$ for our fiducial ejecta model with $\alpha = 1$. The thermalization efficiency decreases with increasing velocity coordinate as the ejecta becomes more diffuse. In the trapped limit, this decrease is driven by adiabatic losses. In the radial field limit, this decrease is driven by particle escape, although there are still significant adiabatic losses. The radial field scenario has lower thermalization efficiency at every velocity coordinate, with the largest differences in the innermost and outermost ejecta.

and $f_{\text{thm}} \propto t^{-n}$ for $t \gg t_{\text{ineff}}$. This form produces a better fit to our simulations than the alternative form $f_{\text{thm}}(t) = [1 + (t/t_{\text{ineff}})]^{-n}$ derived by Kasen & Barnes (2019).

Thermalization becomes inefficient when the timescale for thermalization $t_{\text{thm}} \approx E/\dot{E}|_{\text{coll}} \propto \rho^{-1} \propto M_{\text{ej}}^{-1} v_{\text{ej}}^3 (u/v_{\text{ej}})^{\alpha} t^3$ becomes longer than the timescale for adiabatic expansion $t_{\text{exp}} = t$ (Barnes et al. 2016). Setting $t_{\text{exp}} = t_{\text{thm}}$ and solving for t , we find

$$t_{\text{ineff}} \propto M_{\text{ej}}^{1/2} v_{\text{ej}}^{-3/2} (u/v_{\text{ej}})^{-\alpha/2}. \quad (55)$$

For the asymptotic slope, Barnes et al. (2016) derived a value $n = 2$ for an idealized model where collisional energy losses are independent of energy, the decay spectrum is independent of time, and the energy injection rate declines as $Q_{\text{inj}} \propto t^{-1}$. For a more general model, the asymptotic slope can deviate from this value (Kasen & Barnes 2019).

We divide the ejecta into 32 equal bins in velocity coordinate and fit Equation 54 to the thermalization efficiency integrated across each bin. The integration is necessary to reduce numerical noise. We perform the curve fit in log-log space using least-squares regression as implemented in `scipy.optimize.curve_fit`. In Figure 12, we show the inefficiency time and asymptotic slope as a function of velocity coordinate for many ejecta models, varying each ejecta model parameter separately. We also fit Equation 54 to the thermalization efficiency integrated across all velocity coordinates to get a simplified description of the global thermalization. In this work, we are mostly interested in the spatially dependent thermalization efficiency, but we tabulate the results in Appendix B for completeness.

We show the fiducial ejecta model in black. In the trapped limit, the inefficiency times scales with velocity coordinate as $t_{\text{ineff}} \propto u^{-1/2}$, as expected from Equation 55 with $\alpha = 1$. In the radial field limit, the inefficiency time is shorter at all velocity coordinates, especially in the innermost and outermost ejecta. In the innermost ejecta, this

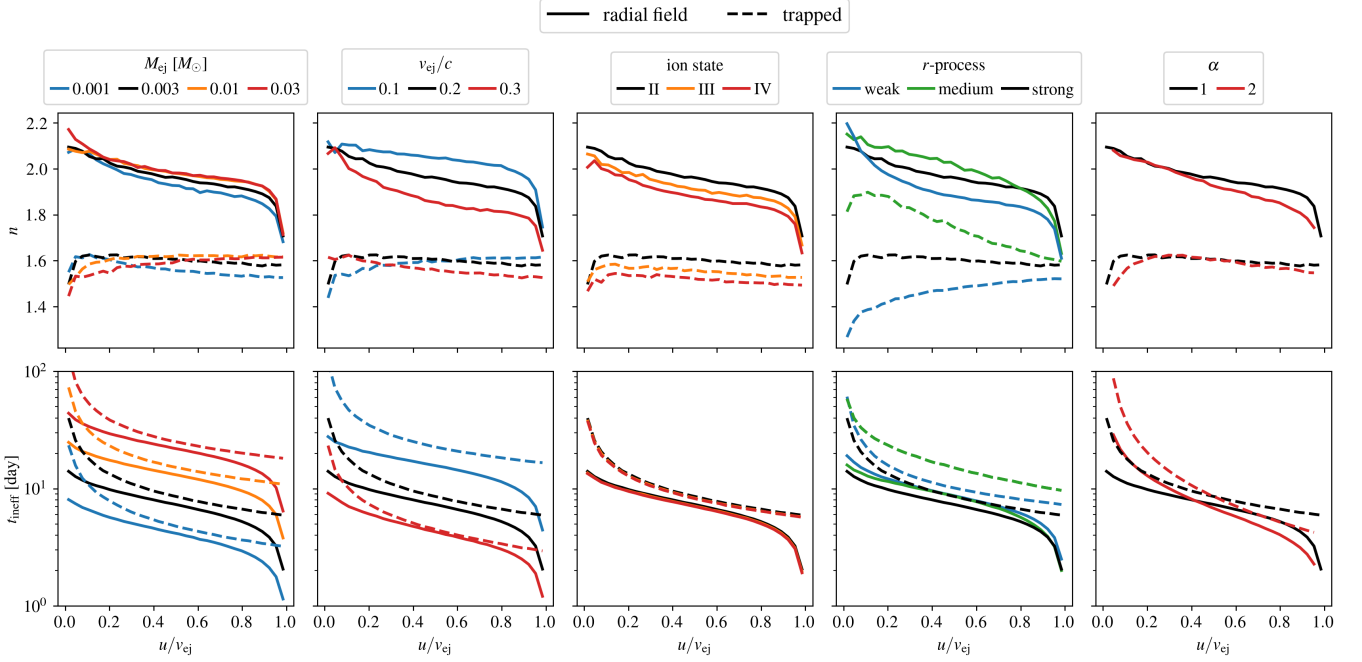


Figure 12. The inefficiency time (bottom panels) and asymptotic slope (top panels) as a function of velocity coordinate, derived by fitting Equation 54 to the thermalization efficiency at each velocity coordinate. In each column, we vary a different ejecta model parameter—ejecta mass (first column), velocity (second column), ionization state (third column), r -process abundance pattern (fourth column), and density profile power-law exponent (fifth column). Each curve is colored by its parameter value in the color bar above the column, with the fiducial ejecta model in black. We show curves in radial magnetic field (solid lines) and trapped (dashed lines) limits. In the trapped limit, the inefficiency time scales with velocity coordinate as $t_{ineff} \propto u^{-1/2}$, as expected from Equation 55 with $\alpha = 1$. In the radial field limit, the inefficiency time is shorter at all velocity coordinates, especially in the innermost and outermost ejecta due to particle transport and escape.

behavior occurs because transport is biased towards larger velocity coordinate where thermalization is less efficient. In the outermost ejecta, this behavior occurs because particles efficiently escape the ejecta.

In the trapped limit, the asymptotic slope is nearly constant across velocity coordinates with a value $n \approx 1.6$. This is lower than the value $n = 2$ from Barnes et al. (2016) due to the more rapid decline in the decay rate $\propto t^{-1.3}$ (Eq. 4) compared to $\propto t^{-1}$ and the time evolution of the decay spectrum (Fig. 3). In the radial field limit, the asymptotic slope is larger, with values $n \approx 1.9$ – 2.0 due to increasing particle escape at late times. The asymptotic slope is smaller in the outer ejecta where particle escape is most efficient.

4.4 Dependence on the ejecta model

The inefficiency time increases with ejecta mass and decreases with ejecta velocity for both transport limits, as expected from Equation 55. The difference in inefficiency time between the transport limits shrinks for larger ejecta velocities because of changes to the escape timescale. At larger velocity coordinate, the transition to free-streaming occurs earlier and the escape time in that phase increases (Sec. 4.1). As a consequence, particles persist in the ejecta longer at late times, enhancing the thermalization efficiency, although this effect is partially mitigated by enhanced relativistic focusing. This enhancement to the late-time thermalization efficiency also explains the shallower asymptotic slopes at larger ejecta velocity.

The inefficiency time is insensitive to the ionization state of the ejecta. However, the asymptotic slope tends to decrease at higher ionization states due to the higher free electron densities in more

ionized ejecta, which enhances the thermalization losses of lower energy β -particles prevalent at late times through Møller scattering (Fig. 6).

The r -process abundance pattern has three effects. First, the abundance pattern changes the stopping power and transport cross section. These quantities are similar for the strong and medium r -process abundances, but are reduced by a factor of a few for the weak r -process due to the smaller ionization losses associated with elements from the first r -process peak.

Second, the abundance pattern changes the time-dependent injection rate (Fig. 2). The injection rate oscillates about an overall power law trend depending on the detailed decay pattern. The timing of these oscillations near the transition to inefficient thermalization has a significant effect on the thermalization efficiency. Relative to the strong r -process injection rate, the medium r -process rate declines more rapidly from 6–30 days and more slowly at ≥ 30 days, while the weak r -process rate declines more rapidly from 3–20 days and more slowly from 20–100 days.

Third, the abundance pattern changes the decay spectrum (Fig. 3). At typical inefficiency times in our simulations of $t_{ineff} \approx 1$ – 10 days, the average decay electron produced by the strong, medium, and weak r -process has an energy around 400 keV, 250 keV, and 200 keV, respectively (Fig. 2).

In the trapped limit, the medium r -process has the longest inefficiency time. This behavior is driven by the more rapid decline in the injection rate at intermediate times, which enhances the thermalization efficiency because delayed deposition from particles injected earlier, when the injection rate was higher, contributes disproportionately relative to the lower instantaneous injection rate. This effect is

partially counterbalanced by the more energetic decay spectrum relative to the strong r -process, which makes thermalization less efficient because the stopping power is lower at higher energies and particles persist in the ejecta for longer durations.

Similarly, the weak r -process also has a longer inefficiency time. However, in the weak r -process case, the effect is additionally counterbalanced by the reduction in stopping power and transport opacity from the atomic physics. The net result is an inefficiency time in between those for the medium and strong r -processes.

In the radial field limit, the inefficiency times for the medium and weak r -processes are closer to the strong r -process value, suggesting that the effects of the abundance pattern are diluted by transport. In particular, the effect of fluctuations in the injection rate may be weaker because particles move to larger velocity coordinate as they thermalize, where for $\alpha = 1$ they make up a smaller fraction of the injected energy.

For a steeper density power-law index $\alpha = 2$ in the trapped limit, the inefficiency time declines more steeply with velocity coordinate as $t_{\text{ineff}} \propto u^{-1}$, following Equation 55. For both transport scenarios, thermalization is more efficient because a greater fraction of the energy is injected at smaller radii where the inefficiency time is the longest.

Even with a relatively limited set of ejecta models, the diversity of thermalization behaviors suggests that results from a single ejecta model should not be interpreted as universal. Aside from the ejecta mass and velocity, thermalization is also sensitive to fluctuations in the energy injection rate relative to the overall power law trend and the density profile of the ejecta. In comparison, thermalization is less sensitive to the ejecta ionization state, so energy deposition can be reasonably modeled without computing the ionization state self-consistently.

4.5 Analytic prescription

Using the same curve-fitting procedure described in Section 4.3, we fit the spatially dependent thermalization efficiency across our series in ejecta mass and velocity with the following equations:

$$f_{\text{thm}} = \ln(1 + \tau)/\tau, \quad \tau \equiv 2(t/t_{\text{ineff}})^{-n} \quad (56)$$

$$t_{\text{ineff}}^{(\text{trp})} = t_{\text{ineff},0} M_{0.003}^{1/2} v_{0.2}^{-3/2} x^{-\alpha/2} \quad (57)$$

$$t_{\text{ineff}}^{(\text{rad})} = v_{0.2}^{1/3} b(x; x_p, r_p, 2/3) t_{\text{ineff}}^{(\text{trp})}, \quad (58)$$

where $M_{0.003} \equiv M_{\text{ej}}/0.003 M_{\odot}$, $v_{0.2} \equiv v_{\text{ej}}/0.2c$, $x \equiv u/v_{\text{ej}}$, the superscripts denote the radial field (rad) and trapped (trp) limits, and $b(x)$ is a normalized beta-profile given by

$$b(x; x_p, r_p, w) \equiv r_p \left(\frac{x}{x_p} \right)^{w x_p} \left(\frac{1-x}{1-x_p} \right)^{w(1-x_p)}. \quad (59)$$

The profile peaks at (x_p, r_p) and its width is controlled by w , which we fix to $w = 2/3$ since it provides a reasonable fit across all models. This choice captures the expected behavior in the radial field limit. The inefficiency time approaches zero at the ejecta edges and approaches the trapped-limit value at intermediate velocity coordinates. The asymptotic slope is roughly independent of ejecta mass and velocity in the trapped limit, and can be approximated by a linear dependence on ejecta velocity in the radial field limit.

In Table 1, we show the resulting fit parameters for models with density power-law slopes of $\alpha = 1$ and $\alpha = 2$. To evaluate the accuracy of this prescription, we compute the logarithmic residuals relative to our Monte Carlo results $\log(f_{\text{thm}}^{(\text{analytic})}/f_{\text{thm}}^{(\text{mc})})$. Across all locations, times, and ejecta models, the median absolute residuals are

Table 1. Fit parameters for Equations 56–58, which describe the thermalization efficiency as a function of time, velocity coordinate (position), ejecta mass, and ejecta velocity. Each row shows the results for models with a different density power-law slope α .

α	$t_{\text{ineff},0}^{(\text{trp})}$ [day]	x_p	r_p	$n^{(\text{trp})}$	$n^{(\text{rad})}$
1	5.65	0.53	0.83	1.58	$2.14 - 0.17(v_{\text{ej}}/0.2c)$
2	4.16	0.59	0.78	1.56	$2.13 - 0.18(v_{\text{ej}}/0.2c)$

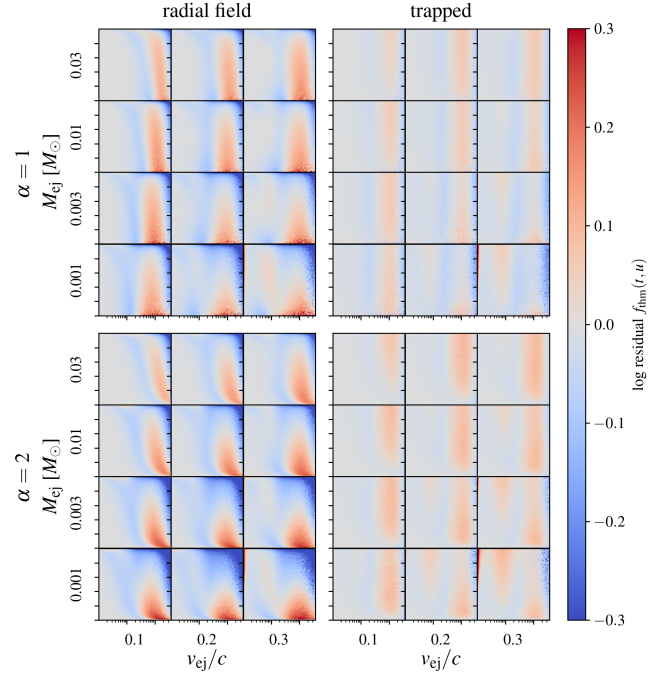


Figure 13. Thermalization efficiency logarithmic residuals $\log(f_{\text{thm}}^{(\text{analytic})}/f_{\text{thm}}^{(\text{mc})})$ for the analytic prescription described by Equations 56–58 at each bin in velocity coordinate and time for different ejecta models in each panel. The x - and y -axes are identical to Figure 9. The top and bottom panel groups show models with density power-law slopes $\alpha = 1$ and $\alpha = 2$ respectively. The left and right panel groups show models in the radial field and trapped limits respectively. Within each panel group, rows correspond to different ejecta masses and columns correspond to different ejecta velocities. In the trapped limit, all models have logarithmic residuals $\lesssim 0.1$ dex at all locations and times. In the radial field limit, the largest residuals ~ 0.2 dex occur in the innermost and outermost ejecta at late times because we approximate the asymptotic slope as independent of velocity coordinate. These results indicate that our prescription is a reasonable approximation across a range of ejecta conditions.

0.037 and 0.018 dex in the radial field and trapped limits respectively. In Figure 13, we plot the residuals at each location and time for all models. In the trapped limit, all models have residuals $\lesssim 0.1$ dex at all locations and times. In the radial field limit, the largest residuals ~ 0.2 dex occur in the innermost and outermost ejecta at late times, mostly because we approximate the asymptotic slope as independent of velocity coordinate.

This prescription provides a simple, computationally cheap approximation for the spatially dependent thermalization efficiency that can be incorporated into semi-analytic and/or radiative-transfer KN emission models. However, it should only be used as a first approximation since, in detail, the thermalization efficiency depends on

the time-dependent nuclear decay rate. In general, we recommend explicit charged particle transport whenever feasible, particularly in multi-dimensional simulations where magnetic field geometry and ejecta structure may differ substantially from the idealized models considered here. We provide β -particle stopping and transport cross sections for use in explicit transport models (see Footnote 4).

4.6 Ejecta ionization structure

The ejecta temperature evolves according to the first law of thermodynamics (Jerkstrand 2011; Pognan et al. 2022a), i.e.

$$\frac{dT}{dt} = \frac{\mathcal{H} - C}{\frac{3}{2}k_B n} - \frac{2T}{t} - \frac{T}{1 + x_{e,\text{thm}}} \frac{dx_{e,\text{thm}}}{dt}, \quad (60)$$

where $\mathcal{H} = f_{\text{thm}}\rho Q_{\text{inj}}$ is the volumetric heating rate, C is the volumetric cooling rate, $n = n_i + n_{e,\text{thm}}$ is the total thermal particle number density, and $x_{e,\text{thm}} \equiv n_{e,\text{thm}}/n_i$ is the free thermal electron number fraction. The second term accounts for adiabatic cooling and the third term accounts for the ionization potential energy reservoir.

In practice, the electron number fraction changes slowly relative to the expansion timescale, so the ionization term is always subdominant to the adiabatic term and we neglect it. Cooling in the nebular phase is dominated by line cooling of heavy r -process elements (Pognan et al. 2022a). Since this quantity is proportional to $n_e n_i$, we define $C \equiv n_e n_i \Lambda$, where Λ is independent of temperature for sufficiently low densities, i.e. $n \lesssim 10^4 \text{ cm}^{-3}$ (Hotokezaka et al. 2021).

We do not model the radiation field, and instead assume that all line photons escape locally. This approximation is reasonable in the nebular phase when the ejecta are optically thin. However, we may underestimate the temperature at early times when the radiation is partially coupled to the gas.

The ionization fractions evolve according to the rate equations (Pognan et al. 2022a)

$$\frac{dx_{i,q}}{dt} = \Gamma_{i,q-1} x_{i,q-1} - (\alpha_{i,q} n_{e,\text{thm}} + \Gamma_{i,q}) x_{i,q} + \alpha_{i,q+1} x_{i,q+1}, \quad (61)$$

where $\Gamma_{i,q}$ and $\alpha_{i,q}$ are the ionization rate and recombination rate coefficient for species (i, q) and $n_{e,\text{thm}}$ is the number density of free thermal electrons given by

$$n_{e,\text{thm}} = \rho N_A \sum_i Y_i \sum_q x_{iq} q. \quad (62)$$

The total cooling function is the sum of contributions from each species,

$$\Lambda = \mu_{\text{mmw}} \sum_i Y_i \sum_q x_{iq} \Lambda_{iq}. \quad (63)$$

For r -process elements, dielectronic recombination (DR) dominates over radiative recombination (RR), sometimes by more than an order-of-magnitude (Hotokezaka et al. 2021; Singh et al. 2025). At typical nebular temperatures 10^{3-4} K, autoionizing states near the ionization threshold contribute to DR, making the rate sensitive to fine structure. Detailed DR calculations for astrophysical applications have been published for an increasing, but still incomplete, sample of r -process elements including Selenium ($Z = 34$), Krypton ($Z = 36$) (Sterling & Witthoef 2011; Sterling 2011), Neodymium (Nd, $Z = 60$) (Hotokezaka et al. 2021), Rubidium ($Z = 37$), Strontium ($Z = 38$), Yttrium ($Z = 39$), Zirconium ($Z = 40$) (Banerjee et al. 2025), Uranium ($Z = 92$) (Ferguson et al. 2026), and individual ion stages of Tellurium ($Z = 52$) and Cerium ($Z = 58$) (Singh et al. 2025).

An accurate calculation of the ejecta temperature and ionization

structure including all r -process elements may soon be possible. In the meantime, we do an illustrative calculation of the ejecta temperature and ionization state for Nd to demonstrate the effects of particle transport and the ionization cascade, leaving a more self-consistent calculation to future work. For simplicity, we assume that all ions are Nd, neglecting the coupling between ionization states of different elements via the shared pool of free electrons. We only include contributions to ionization and heating from β -particles, neglecting contributions from other decay products like α -particles and fission fragments. We neglect photoionization, which is only expected to dominate at early times when the radiation temperature $\gtrsim 10^4$ K (Brethauer et al. 2026).

We use the temperature-dependent DR rate coefficients and cooling functions for Nd II, Nd III, and Nd IV from Figures 3 and 6 of Hotokezaka et al. (2021) respectively. For Nd I and Nd V, we set the cooling function to that for Nd II and Nd IV respectively. For Nd I, we set the DR rate coefficient equal to 1/4 that for Nd II. We use an analytic formula for the Case B RR rate coefficients from Axelrod (1980). Higher ion stages have higher DR rates and cool less efficiently. For all ion stages, the cooling function increases monotonically with temperature.

At each velocity coordinate in our fiducial ejecta model, we integrate Equations 60 and 61, taking the heating and per-species ionization rates from our Monte Carlo simulation. The equations are stiff and non-linear, so at each integration step, we iteratively compute the temperature and free electron density and take backward-Euler updates until convergence. The results are not sensitive to the initial conditions because, at early times, the thermal and ionization equilibrium timescales are short, so the ejecta is well described by a steady-state solution. Time-dependent effects only become important at late times as the equilibrium timescales grow (Pognan et al. 2022a).

In Figure 14, we show the ejecta temperature and Nd ionization state for both transport scenarios, similar to Figure 3 of Brethauer et al. (2026). We also show the inefficiency time and the time when adiabatic cooling dominates at each velocity coordinate. In agreement with Brethauer et al. (2026), we find that the nebular ejecta has an inverted ionization structure due to less efficient recombination in the more diffuse outer ejecta and multiple ionization stages coexist at each location. Because our fiducial ejecta model ($M_{\text{ej}} = 0.003 M_{\odot}$, $v_{\text{ej}} = 0.2c$) produces lower densities than the ejecta model considered by Brethauer et al. (2026) ($M_{\text{ej}} = 0.03 M_{\odot}$, $v_{\text{ej}} = 0.1c$), our ejecta is more ionized than theirs, with Nd IV and Nd V dominating after ~ 10 days. Our results also deviate from theirs at early times when photoionization dominates over ionization from β -particles and photon absorption contributes significantly to heating.

The thermal evolution can be understood following the logic of Pognan et al. (2022a). The line cooling rate scales as $C_{\text{line}} \propto \rho^2 \Lambda$. In the steady state and ignoring adiabatic cooling, we have $\mathcal{H} = C_{\text{line}}$, so the cooling function scales as $\Lambda \propto \rho^{-1} f_{\text{thm}} Q_{\text{inj}} \propto u^{\alpha} t^3 f_{\text{thm}} Q_{\text{inj}}$. Even though the energy injection rate and thermalization efficiency decrease over time, the density decreases faster due to homologous expansion, which requires the temperature to increase to support a higher equilibrium cooling function.

Initially, f_{thm} is approximately constant, so the cooling function increases rapidly $\Lambda \propto t^{1.7}$ and the ejecta heats up, reaching $\gtrsim 10000$ K after an inefficiency time. These temperatures are significantly hotter than models that neglect charged-particle ionization, for which the nebular-phase ejecta are mostly neutral and cool more efficiently (Brethauer et al. 2026; Fontes et al. 2026).

After a couple of inefficiency times, f_{thm} decreases rapidly, counterbalancing the falling density and causing the temperature to level

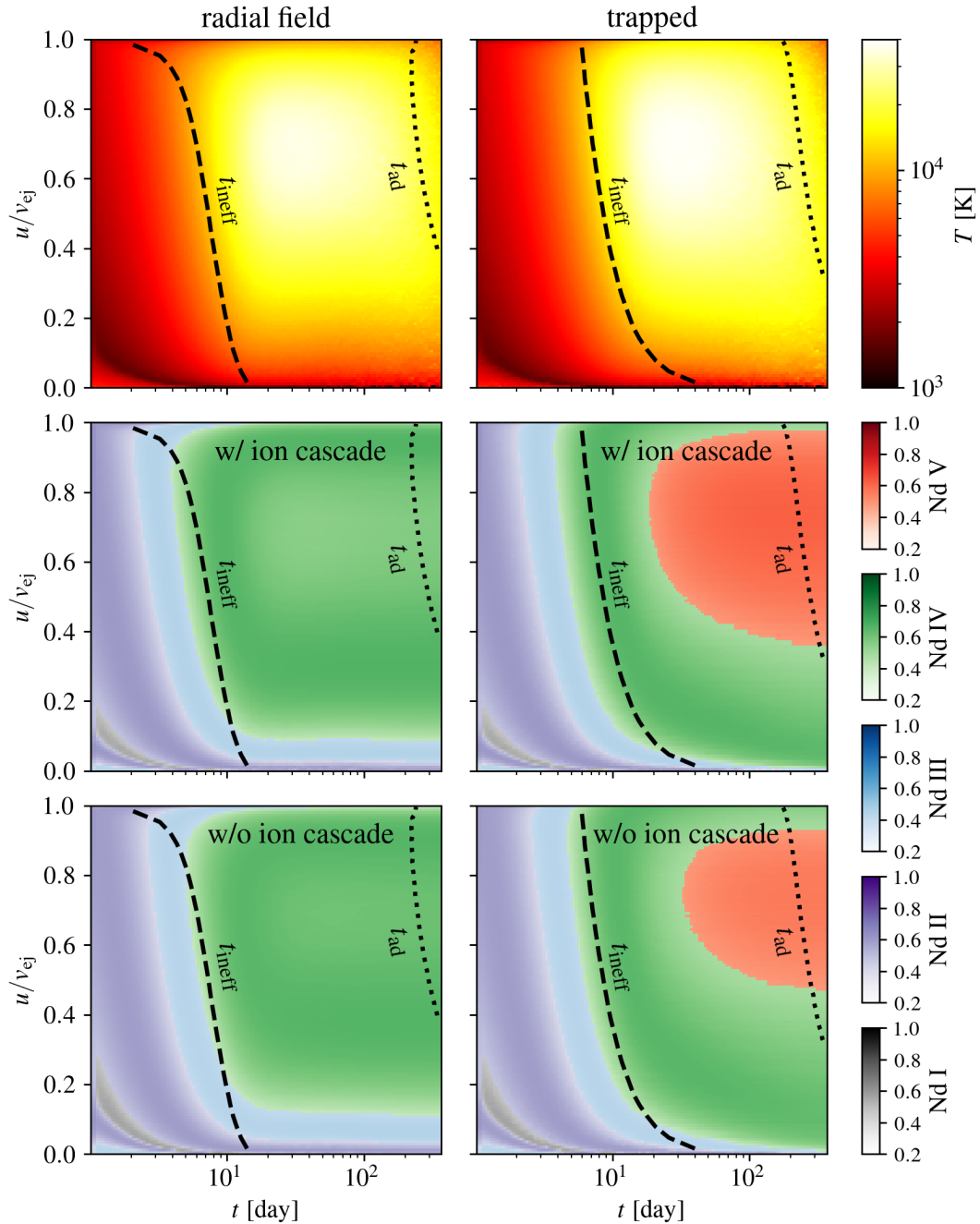


Figure 14. The temperature (first row) and ionization state (second row) of Neodymium ($Z = 60$) at each bin in velocity coordinate and time in our fiducial ejecta model in the radial magnetic field (left column) and trapped (right column) limits. Color represents the dominant ionization species, with intensity representing the fraction of that element that is in the dominant ionization state. Nd I, Nd II, Nd III, Nd IV, and Nd V are represented by black, purple, blue, green, and red respectively. In each panel, we plot the time at which thermalization starts to become inefficient t_{ineff} (dashed black lines) and the time at which adiabatic cooling dominates t_{ad} (dotted black lines) at each velocity coordinate. In agreement with [Brethauer et al. \(2026\)](#), we find that the nebular ejecta has an inverted ionization structure due to less efficient recombination in the more diffuse outer ejecta and multiple ionization stages coexist at each location. Radial fields lead to a lower ionization state because particle escape lowers the ionization and heating rates. We also show the ionization state without the ionization cascade (third row; see Sec. 2.6), which lowers the ionization state throughout the ejecta.

off. At late times $\gtrsim 100$ day, adiabatic cooling starts to contribute significantly and the outer ejecta cools.

The same argument explains why the temperature peaks at intermediate velocity coordinates at a given time. In the inner ejecta, the equilibrium cooling function shifts to lower values due to the higher

density, while in the outer ejecta, the function shifts to lower values due to less efficient thermalization.

As the temperature rises, the typical ionization stage increases, with the dominant species transitioning from Nd II/III to Nd IV/V. Radial fields promote particle escape, which lowers the ionization and heating rates, which also leads to lower ejecta temperatures and

recombination rates. The net result is lower ionization stages throughout the ejecta. The dominant ion stage at late times is Nd IV in the radial field limit, compared to Nd V in the trapped limit. On average, the mean ion charge in corresponding bins is 0.21 lower in the radial field limit than in the trapped limit. Transport physics affects the ionization state most strongly in the innermost and outermost ejecta, where it also has the strongest impact on thermalization efficiency (Fig. 11).

We also show the ionization state without the ionization cascade (see Sec. 2.6), which lowers the ionization state throughout the ejecta. On average, the mean ion charge in corresponding bins is 0.15 lower when the ionization cascade is not included in the radial field limit. The effect is strongest in the inner ejecta, where more energy goes into the cascade. This calculation demonstrates that transport physics and the ionization cascade are necessary pieces for an accurate nebular-phase ionization structure.

5 CONCLUSIONS

We revisit the thermalization and transport of β -particles, which carry most of the decay energy that powers KNe light curves. For thermalization, we use evaluated atomic physics data to estimate per-species contributions to the stopping power, transport opacity, and ionization cross section, which we make available online (see Footnote 4). For transport, we develop a fully relativistic framework for particle transport in a spherically symmetric, homologously expanding ejecta, considering two limiting magnetic-field geometries: particles moving through coherent radial magnetic fields and particles that are completely trapped.

We study the impact of particle transport on thermalization across a range of ejecta models, varying the mass, velocity, ionization state, r -process abundance pattern, and density profile power-law. Overall, we find that charged-particle transport and realistic atomic physics significantly impact thermalization and ejecta ionization structure, and should be incorporated into the next generation of KN models. Our main findings are as follows:

- *β decay rates and spectra:* Non-isochronic decays enhance the overall decay rate relative to the steady-state assumption. Variations in the dominant radioactive nuclide produce shifts in the decay spectra and fluctuations in decay rate relative to the overall power-law trend, which can impact the thermalization efficiency.
- *Stopping power and transport opacity:* At MeV energies, electron impact ionization (EII) and excitation dominate energy loss, while Coulomb interactions with ions dominate scattering. At lower energies reached during thermalization, energy loss and scattering are instead dominated by Coulomb interactions with free thermal electrons (Møller scattering). At higher ionization stages, EII contributions become weaker and Møller contributions become stronger.
- *Secondary electrons:* A single β -particle can ionize thousands of atoms before thermalizing. These ionizations produce a large population of secondary electrons with typical energies ~ 100 eV and a high-energy tail. Ionizations by secondary electrons result in an ionization cascade that contributes significantly to the EII cross section. The cascade contribution increases with incident electron energy, becoming similar to the primary contribution at 1 MeV.
- *Charged particle transport:* As charged particles travel through the ejecta, they lose energy due to collisions and adiabatic expansion of the ejecta. The 1D transport equations for a charged particle in a coherent radial magnetic field are mathematically equivalent to those for an unmagnetized particle because the magnetic mirror force has

the same effect as the rotation of the radial unit vector along a straight-line trajectory. At early times, particles thermalize locally in space and time. At intermediate times, particles persist in the ejecta and thermalize non-locally, increasingly escaping as scattering becomes less efficient. At late times, particles escape before most of their energy thermalizes. Particle escape becomes increasingly important relative to adiabatic losses during the diffusive transport phase, but stalls relative to adiabatic losses during the free-streaming transport phase.

- *Thermalization efficiency:* Particle transport and escape reduce thermalization efficiency, especially in the innermost and outermost ejecta, making the efficiency more uniform across the ejecta compared to local-deposition models. In the trapped limit, particles persist in the ejecta for longer, so energy loss is driven by adiabatic expansion rather than particle escape. Thermalization efficiencies are sensitive to ejecta mass and velocity, as well as r -process abundance pattern and density power-law slope. However, they are less sensitive to ejecta ionization state, so energy deposition can be reasonably modeled without computing the ionization state self-consistently.

- *Analytic prescription:* At each Lagrangian position in the ejecta, we describe the thermalization efficiency $f_{\text{thm}}(t)$ with an analytic formula (Eq. 54) parameterized by t_{ineff} , the time at which thermalization starts to become inefficient, and n , the asymptotic slope. Typical values are $t_{\text{ineff}} \sim 10$ days and $n \simeq 1.6$. We provide formulae for t_{ineff} and n as a function of Lagrangian position and ejecta model parameters for use in future light curve calculations (Eqs. 56–58, Table 1). This prescription is only approximate, so we recommend explicit charged-particle transport whenever feasible.

- *Ejecta ionization structure:* As an illustrative example, we use the rate equations to compute the ionization structure of Neodymium for our fiducial ejecta model. In agreement with Brethauer et al. (2026), we find that the nebular ejecta has an inverted ionization structure due to less efficient recombination in the more diffuse outer ejecta and multiple ionization stages coexist at each location. Radial magnetic fields lead to a lower ionization state because particle escape lowers the ionization and heating rates. On the other hand, including ionization contributions from the ionization cascade raises the ionization state throughout the ejecta.

We focus on β -particles, but α -particles and fission fragments also contribute significantly to heating and ionization, especially at late times, despite carrying a smaller fraction of the nuclear energy (Barnes et al. 2016). Recently, Van den Berg & Hotokezaka (2026) analyzed these decay products in detail. Our results could be integrated with theirs to provide a more complete description of thermalization and ionization. The peak-to-tail luminosity in the KN light curve may be sensitive to the relative contributions of different decay products, which can help constrain ejecta composition (Barnes et al. 2016).

Our illustrative calculation of the ejecta ionization structure should also be coupled to a radiative transfer model (as done in Brethauer et al. 2026) to include photoionization and ionization by recombination photons (Van den Berg & Hotokezaka 2026). In addition, our calculation should be updated to include the ionization and excitation balance for all species, as done in Ricigliano et al. (2025) for the study of r -process elements in supernova nebulae. The resulting radiation field and ejecta ionization structure could then be used to forward model observables.

We only consider particle transport for highly idealized magnetic-field geometries. Although we expect other magnetic field geometries to produce thermalization efficiencies in between our two limiting cases, there may be new behaviors that we do not capture due to

spatially and temporally dependent magnetization, particle energization by diffusive shock acceleration, or collective plasma effects like the streaming instability. Future work should explore charged particle transport in realistic magnetic-field geometries and assess these possibilities using kinetic or hybrid approaches.

We also expect thermalization to be affected by deviations from spherical symmetry, since realistic merger ejecta exhibit angular variations in density, composition, and velocity structure (Kasen et al. 2015; Wollaeger et al. 2018; Bulla 2019; Korobkin et al. 2021). Thermalization may be less efficient if transport can move decay products to more diffuse polar regions. These effects should also be explored in future work.

ACKNOWLEDGEMENTS

ZA would like to thank Gian Luca Delzanno, Robert Ewart, Philipp Kempfski, and Eliot Quataert for helpful conversations.

This material is based upon work supported by the U.S. Department of Energy, Office of Science, Office of Advanced Scientific Computing Research, Department of Energy Computational Science Graduate Fellowship under Award Number DE-SC0024386.

This report was prepared as an account of work sponsored by an agency of the United States Government. Neither the United States Government nor any agency thereof, nor any of their employees, makes any warranty, express or implied, or assumes any legal liability or responsibility for the accuracy, completeness, or usefulness of any information, apparatus, product, or process disclosed, or represents that its use would not infringe privately owned rights. Reference herein to any specific commercial product, process, or service by trade name, trademark, manufacturer, or otherwise does not necessarily constitute or imply its endorsement, recommendation, or favoring by the United States Government or any agency thereof. The views and opinions of authors expressed herein do not necessarily state or reflect those of the United States Government or any agency thereof.

This work was supported by the U.S. Department of Energy through the Los Alamos National Laboratory and approved for public release under unlimited release tracking number LA-UR-26-25420. Los Alamos National Laboratory is operated by Triad National Security, LLC, for the National Nuclear Security Administration of U.S. Department of Energy (contract no. 89233218CNA000001).

The simulations presented in this article were performed on computational resources managed and supported by Princeton Research Computing, a consortium of groups including the Princeton Institute for Computational Science and Engineering (PICSciE) and the Office of Information Technology's High Performance Computing Center and Visualization Laboratory at Princeton University.

DATA AVAILABILITY

Our atomic physics data, adapted from the EEDL database, are available online (see Footnote 4). These data include per-species contributions to the stopping, transport, and electron impact ionization cross sections, as well as combined cross sections using our strong r -process abundance pattern at 30 days post-merger. The Monte Carlo data can be provided upon reasonable request to the corresponding author.

REFERENCES

- Abbott B. P., et al., 2017a, *Nature*, **551**, 85
 Abbott B. P., et al., 2017b, *ApJ*, **848**, L12
 Axelrod T. S., 1980, PhD thesis, University of California, Santa Cruz
 Banerjee S., Jerkstrand A., Badnell N., Pognan Q., Ferguson N., Grumor J., 2025, *arXiv e-prints*, p. arXiv:2501.18345
 Barnes J., Kasen D., 2013, *ApJ*, **775**, 18
 Barnes J., Kasen D., Wu M.-R., Martínez-Pinedo G., 2016, *ApJ*, **829**, 110
 Barnes J., Zhu Y. L., Lund K. A., Sprouse T. M., Vassh N., McLaughlin G. C., Mumpower M. R., Surman R., 2021, *ApJ*, **918**, 44
 Bauswein A., Goriely S., Janka H. T., 2013, *ApJ*, **773**, 78
 Bethe H., 1930, *Annalen der Physik*, **397**, 325
 Bethe H., Heitler W., 1934, *Proceedings of the Royal Society of London Series A*, **146**, 83
 Brethauer D., Kasen D., Margutti R., Chornock R., 2026, *ApJ*, **996**, 64
 Bulla M., 2019, *MNRAS*, **489**, 5037
 Bursalf F. H., 1996, *Applied Mathematics and Computation*, **77**, 213
 Chan K.-W., Lingenfelter R. E., 1993, *ApJ*, **405**, 614
 Chiba K., Tanaka M., Wanajo S., Fujibayashi S., Kawaguchi K., Hotokezaka K., 2026, *arXiv e-prints*, p. arXiv:2604.05703
 Cohen M. H., 1961, *Physical Review*, **123**, 711
 Colgate S. A., Petschek A. G., Kriese J. T., 1980, *ApJ*, **237**, L81
 Côté B., et al., 2018, *ApJ*, **855**, 99
 Cowan R. D., 1981, *The theory of atomic structure and spectra*. Berkeley: University of California Press
 Cowperthwaite P. S., et al., 2017, *ApJ*, **848**, L17
 Cullen D. E., 2017, Technical Report IAEA-NDS-226, A Survey of Electron Cross Section Data for use in EPICS 2017. IAEA (Int. Atomic Energy Agency), 1466 Hudson Way, Livermore, CA, 94550
 Dalcín L., Paz R., Storti M., 2005, *Journal of Parallel and Distributed Computing*, **65**, 1108
 Delzanno G. L., Roytershteyn V., 2019, *Journal of Geophysical Research: Space Physics*, **124**, 7543
 Dessart L., Ott C. D., Burrows A., Rosswog S., Livne E., 2009, *ApJ*, **690**, 1681
 Dickel J. R., Milne D. K., 1976, *Australian Journal of Physics*, **29**, 435
 Drout M. R., et al., 2017, *Science*, **358**, 1570
 Dubner G., Giacani E., 2015, *A&ARv*, **23**, 3
 Eichler D., Livio M., Piran T., Schramm D. N., 1989, *Nature*, **340**, 126
 Even W., et al., 2020, *ApJ*, **899**, 24
 Farrell W., Goertz C., 1990, *Planetary and Space Science*, **38**, 373
 Feng Y., Korobkin O., Most E. R., Smith A. F., Fontes C. J., 2026, *arXiv e-prints*, p. arXiv:2605.03947
 Ferguson N., Jerkstrand A., Banerjee S., O'Mullane M. G., Badnell N. R., 2026, *arXiv e-prints*, p. arXiv:2606.11748
 Fong W., Berger E., 2013, *ApJ*, **776**, 18
 Fong W.-f., et al., 2022, *ApJ*, **940**, 56
 Fontes C. J., et al., 2015, *Journal of Physics B Atomic Molecular Physics*, **48**, 144014
 Fontes C. J., Fryer C. L., Hungerford A. L., Wollaeger R. T., Korobkin O., 2020, *MNRAS*, **493**, 4143
 Fontes C. J., Vieira N., Fryer C. L., Kathirgamaraju A., Korobkin O., Ristić M., Wollaeger R. T., 2026, *ApJ*, **1003**, 89
 Freiburghaus C., Rosswog S., Thielemann F. K., 1999, *ApJ*, **525**, L121
 Fryer C. L., et al., 2024, *ApJ*, **961**, 9
 Goldstein A., et al., 2017, *ApJ*, **848**, L14
 Goriely S., Bauswein A., Janka H.-T., 2011, *ApJ*, **738**, L32
 Grossman D., Korobkin O., Rosswog S., Piran T., 2014, *MNRAS*, **439**, 757
 Harker K. J., Banks P. M., 1984, *Radio Science*, **19**, 454
 Hotokezaka K., Nakar E., 2020, *ApJ*, **891**, 152
 Hotokezaka K., Kiuchi K., Kyutoku K., Okawa H., Sekiguchi Y.-i., Shibata M., Taniguchi K., 2013, *Phys. Rev. D*, **87**, 024001
 Hotokezaka K., Wanajo S., Tanaka M., Bamba A., Terada Y., Piran T., 2016, *MNRAS*, **459**, 35
 Hotokezaka K., Sari R., Piran T., 2017, *MNRAS*, **468**, 91
 Hotokezaka K., Tanaka M., Kato D., Gaigalas G., 2021, *MNRAS*, **506**, 5863
 Itzykson C., Zuber J. B., 1980, *Quantum Field Theory*. International Series

- In Pure and Applied Physics, McGraw-Hill, New York
- Jerkstrand A., 2011, PhD thesis, Stockholm University
- Kasen D., Barnes J., 2019, *ApJ*, **876**, 128
- Kasen D., Badnell N. R., Barnes J., 2013, *ApJ*, **774**, 25
- Kasen D., Fernández R., Metzger B. D., 2015, *MNRAS*, **450**, 1777
- Kasen D., Metzger B., Barnes J., Quataert E., Ramirez-Ruiz E., 2017, *Nature*, **551**, 80
- Kasliwal M. M., et al., 2017, *Science*, **358**, 1559
- Kawaguchi K., Shibata M., Tanaka M., 2020, *ApJ*, **889**, 171
- Kiuchi K., Cerdá-Durán P., Kyutoku K., Sekiguchi Y., Shibata M., 2015, *Phys. Rev. D*, **92**, 124034
- Kiuchi K., Kyutoku K., Sekiguchi Y., Shibata M., 2018, *Phys. Rev. D*, **97**, 124039
- Koch H. W., Motz J. W., 1959, *Reviews of Modern Physics*, **31**, 920
- Koopmans T., 1934, *Physica*, **1**, 104
- Korobkin O., Rosswog S., Arcones A., Winteler C., 2012, *MNRAS*, **426**, 1940
- Korobkin O., et al., 2021, *ApJ*, **910**, 116
- Kulsrud R. M., 2005, Plasma Physics for Astrophysics
- Kyutoku K., Ioka K., Okawa H., Shibata M., Taniguchi K., 2015, *Phys. Rev. D*, **92**, 044028
- Lam S. K., Pitrou A., Seibert S., 2015, in Proceedings of the Second Workshop on the LLVM Compiler Infrastructure in HPC. LLVM '15. Association for Computing Machinery, New York, NY, USA, doi:10.1145/2833157.2833162, <https://doi.org/10.1145/2833157.2833162>
- Lattimer J. M., Schramm D. N., 1974, *ApJ*, **192**, L145
- Li L.-X., Paczyński B., 1998, *ApJ*, **507**, L59
- Lotz W., 1967, *Zeitschrift für Physik*, **206**, 205
- Lund K. A., Engel J., McLaughlin G. C., Mumpower M. R., Ney E. M., Surman R., 2023, *ApJ*, **944**, 144
- Margalit B., Metzger B. D., 2017, *ApJ*, **850**, L19
- McKenzie J. F., 1967, *Physics of Fluids*, **10**, 2680
- McLaughlin G. C., Fuller G. M., Wilson J. R., 1996, *The Astrophysical Journal*, **472**, 440–451
- Metzger B. D., 2019, *Living Reviews in Relativity*, **23**, 1
- Metzger B. D., et al., 2010, *MNRAS*, **406**, 2650
- Miller J. M., et al., 2019, *Physical Review D*, **100**
- Milne D. K., 1987, *Australian Journal of Physics*, **40**, 771
- Milne P. A., The L. S., Leising M. D., 1999, *ApJS*, **124**, 503
- Misch G. W., Mumpower M. R., 2024, *European Physical Journal Special Topics*, **233**, 1075
- Misch G. W., Ghorui S. K., Banerjee P., Sun Y., Mumpower M. R., 2021a, *ApJS*, **252**, 2
- Misch G. W., Sprouse T. M., Mumpower M. R., 2021b, *ApJ*, **913**, L2
- Møller C., 1932, *Annalen der Physik*, **406**, 531
- Möller P., Mumpower M. R., Kawano T., Myers W. D., 2019, *Atomic Data and Nuclear Data Tables*, **125**, 1
- Mougeot X., 2015a, *Phys. Rev. C*, **91**, 055504
- Mougeot X., 2015b, *Phys. Rev. C*, **92**, 059902
- Mumpower M. R., Kawano T., Möller P., 2016, *Phys. Rev. C*, **94**, 064317
- Mumpower M., Kawano T., Korobkin O., Misch G., Sprouse T., 2025, *Atomic Data and Nuclear Data Tables*, p. 101736
- Narayan R., Paczynski B., Piran T., 1992, *ApJ*, **395**, L83
- Nedora V., Bernuzzi S., Radice D., Perego A., Endrizzi A., Ortiz N., 2019, *ApJ*, **886**, L30
- Nedora V., et al., 2021, *ApJ*, **906**, 98
- Nissanke S., Holz D. E., Dalal N., Hughes S. A., Sievers J. L., Hirata C. M., 2013, *arXiv e-prints*, p. [arXiv:1307.2638](https://arxiv.org/abs/1307.2638)
- Paczynski B., 1986, *ApJ*, **308**, L43
- Perego A., Rosswog S., Cabezón R. M., Korobkin O., Käppeli R., Arcones A., Liebendörfer M., 2014, *MNRAS*, **443**, 3134
- Pian E., et al., 2017, *Nature*, **551**, 67
- Pognan Q., Jerkstrand A., Grumer J., 2022a, *MNRAS*, **510**, 3806
- Pognan Q., Jerkstrand A., Grumer J., 2022b, *MNRAS*, **513**, 5174
- Pognan Q., Grumer J., Jerkstrand A., Wanajo S., 2023, *MNRAS*, **526**, 5220
- Pognan Q., Wu M.-R., Martínez-Pinedo G., da Silva R. F., Jerkstrand A., Grumer J., Flörs A., 2025, *MNRAS*, **536**, 2973
- Price D. J., Rosswog S., 2006, *Science*, **312**, 719
- Radice D., Perego A., Hotokezaka K., Fromm S. A., Bernuzzi S., Roberts L. F., 2018, *ApJ*, **869**, 130
- Ricigliano G., Hotokezaka K., Arcones A., 2025, *MNRAS*, **543**, 2534
- Roberts L. F., Kasen D., Lee W. H., Ramirez-Ruiz E., 2011, *ApJ*, **736**, L21
- Rosswog S., 2013, *Philosophical Transactions of the Royal Society of London Series A*, **371**, 20120272
- Rosswog S., Korobkin O., 2024, *Annalen der Physik*, **536**, 2200306
- Rosswog S., Liebendörfer M., Thielemann F. K., Davies M. B., Benz W., Piran T., 1999, *A&A*, **341**, 499
- Rosswog S., Korobkin O., Arcones A., Thielemann F. K., Piran T., 2014, *MNRAS*, **439**, 744
- Rosswog S., Sollerman J., Feindt U., Goobar A., Korobkin O., Wollaeger R., Fremling C., Kasliwal M. M., 2018, *A&A*, **615**, A132
- Savchenko V., et al., 2017, *ApJ*, **848**, L15
- Sekiguchi Y., Kiuchi K., Kyutoku K., Shibata M., Taniguchi K., 2016, *Phys. Rev. D*, **93**, 124046
- Siegert T., 2023, *Ap&SS*, **368**, 27
- Singh S., Harman Z., Keitel C. H., 2025, *A&A*, **700**, A110
- Smartt S. J., et al., 2017, *Nature*, **551**, 75
- Sneppen A., Watson D., Damgaard R., Heintz K. E., Vieira N., Väisänen P., Mahoro A., 2024, *A&A*, **690**, A398
- Sprouse T. M., Mumpower M. R., Surman R., 2021, *Phys. Rev. C*, **104**, 015803
- Sprouse T. M., Misch G. W., Mumpower M. R., 2022, *ApJ*, **929**, 22
- Sprouse T. M., Lund K. A., Miller J. M., McLaughlin G. C., Mumpower M. R., 2024, *ApJ*, **962**, 79
- Sterling N. C., 2011, *A&A*, **533**, A62
- Sterling N. C., Witthoef M. C., 2011, *A&A*, **529**, A147
- Tanaka M., Hotokezaka K., 2013, *ApJ*, **775**, 113
- Tanaka M., et al., 2017, *PASJ*, **69**, 102
- Tanvir N. R., et al., 2017, *ApJ*, **848**, L27
- Trkov A., Brown D. A., 2018, doi:10.2172/1425114
- Van den Berg L. N., Hotokezaka K., 2026, *arXiv e-prints*, p. [arXiv:2605.26613](https://arxiv.org/abs/2605.26613)
- Versharen D., et al., 2026, *arXiv e-prints*, p. [arXiv:2605.04293](https://arxiv.org/abs/2605.04293)
- Vink J., et al., 2022, *ApJ*, **938**, 40
- Wanajo S., Sekiguchi Y., Nishimura N., Kiuchi K., Kyutoku K., Shibata M., 2014, *ApJ*, **789**, L39
- Waxman E., Ofek E. O., Kushnir D., Gal-Yam A., 2018, *MNRAS*, **481**, 3423
- Waxman E., Ofek E. O., Kushnir D., 2019, *ApJ*, **878**, 93
- Wollaeger R. T., et al., 2018, *MNRAS*, **478**, 3298
- Wollaeger R. T., et al., 2021, *ApJ*, **918**, 10
- Wollaeger R. T., et al., 2024, *ApJ*, **966**, 177
- Wu Z., Ricigliano G., Kashyap R., Perego A., Radice D., 2022, *MNRAS*, **512**, 328

APPENDIX A: PDF INTERPOLATION METHOD

The EEDL database provides differential EII cross sections in the secondary electron energy and differential Mott scattering cross sections in scattering angle at a set of discrete energies. To determine these differential cross section at an arbitrary electron energy, we must interpolate a probability distribution function (PDF) from the given PDFs. Consider a tabulated dataset $\{(t_0, p_0(x)), (t_1, p_1(x)), \dots, (t_N, p_N(x))\}$ where $p_i(x)$ is the PDF of x for $t = t_i$. It would be convenient to interpolate between the tabulated PDFs using the standard interpolation formula

$$p_t(x) = (1 - \alpha)p_i(x) + \alpha p_{i+1}(x), \quad (\text{A1})$$

where $\alpha = (t - t_i)/(t_{i+1} - t_i)$ is the interpolation parameter. However, this produces undesirable results because $p_i(x)$ and $p_{i+1}(x)$ may be concentrated in different regions of the state space (Bursal 1996). For example, one might incorrectly obtain a bimodal distribution by interpolating between two unimodal distributions.

Table B1. The inefficiency time t_{ineff} and asymptotic slope n for ejecta models in our series in ejecta mass and velocity with density power-law slope $\alpha = 1$, determined by fitting Equation 54 to the thermalization efficiency integrated over velocity coordinate. We show values in the radial magnetic field (superscript rad) and trapped (superscript trp) limits. The fiducial model is bolded.

$M_{\text{ej}} [M_{\odot}]$	v_{ej}/c	$t_{\text{ineff}}^{(\text{rad})}$ [day]	$n^{(\text{rad})}$	$t_{\text{ineff}}^{(\text{trp})}$ [day]	$n^{(\text{trp})}$
0.001	0.1	7.53	1.99	12.5	1.59
0.003	0.1	12.7	1.99	20.8	1.58
0.01	0.1	22.5	1.98	36.5	1.53
0.03	0.1	38.9	1.99	63.5	1.49
0.001	0.2	3.36	1.89	4.32	1.53
0.003	0.2	5.91	1.91	7.74	1.58
0.01	0.2	10.6	1.93	13.8	1.59
0.03	0.2	17.8	1.92	22.9	1.57
0.001	0.3	1.91	1.78	2.14	1.49
0.003	0.3	3.49	1.82	4.02	1.53
0.01	0.3	6.50	1.86	7.60	1.58
0.03	0.3	11.1	1.87	12.9	1.59

Table B2. Same as Table B1, but with density power-law slope $\alpha = 2$.

$M_{\text{ej}} [M_{\odot}]$	v_{ej}/c	$t_{\text{ineff}}^{(\text{rad})}$ [day]	$n^{(\text{rad})}$	$t_{\text{ineff}}^{(\text{trp})}$ [day]	$n^{(\text{trp})}$
0.001	0.1	9.98	1.75	16.6	1.22
0.003	0.1	16.8	1.73	28.3	1.22
0.01	0.1	29.9	1.71	51.2	1.22
0.03	0.1	51.3	1.68	89.7	1.22
0.001	0.2	4.76	1.71	5.74	1.18
0.003	0.2	8.07	1.70	10.1	1.21
0.01	0.2	14.3	1.69	18.4	1.22
0.03	0.2	23.9	1.66	31.4	1.22
0.001	0.3	2.95	1.67	2.92	1.15
0.003	0.3	5.05	1.66	5.35	1.18
0.01	0.3	9.01	1.65	9.99	1.20
0.03	0.3	15.1	1.63	17.2	1.22

Instead, we interpolate the inverse cumulative distribution functions (CDF), or quantile functions. If $F_i(x)$ is the CDF of x at $t = t_i$, then $F_t(x)$ is

$$F_t^{-1}(q) = (1 - \alpha)F_i^{-1}(q) + \alpha F_{i+1}^{-1}(q). \quad (\text{A2})$$

The CDF is given by inverting $F_t^{-1}(q)$ and the PDF is given by differentiation $p_t(x) = dF_t(x)/dx$.

As a proof-of-concept, consider interpolating between two delta functions $\delta(x - x_0)$ and $\delta(x - x_1)$. The inverse CDFs are $F_0^{-1}(\xi) = x_0$ and $F_1^{-1}(\xi) = x_1$ respectively. Using Equation A2, the interpolated inverse CDF is $x_i(\xi) = (1 - \alpha)x_0 + \alpha x_1$. This implies that the interpolated PDF is $\delta(x - x_i)$, which matches our intuitive expectation.

APPENDIX B: THERMALIZATION EFFICIENCY FIT PARAMETERS

In this section, we provide tables for the inefficiency time and asymptotic slope for all ejecta models, determined by fitting Equation 54 to the thermalization efficiency integrated over velocity coordinate. In Tables B1 and B2, we show results for our series in ejecta mass and velocity with density power-law exponents $\alpha = 1$ and $\alpha = 2$ respectively. In Table B3, we show results for our series in ejecta ionization stage and r -process abundance pattern.

Table B3. Same as Table B1, but for our series in ejecta ionization state and r -process abundance pattern. The fiducial model is bolded.

ion stage	r -process	$t_{\text{ineff}}^{(\text{rad})}$ [day]	$n^{(\text{rad})}$	$t_{\text{ineff}}^{(\text{trp})}$ [day]	$n^{(\text{trp})}$
II	weak	7.04	1.83	9.27	1.47
III	weak	7.32	1.79	9.80	1.41
IV	weak	7.76	1.76	10.5	1.38
II	medium	6.65	1.93	13.3	1.68
III	medium	6.37	1.88	13.0	1.62
IV	medium	6.33	1.84	13.2	1.59
II	strong	5.91	1.91	7.74	1.58
III	strong	5.74	1.87	7.50	1.53
IV	strong	5.66	1.83	7.43	1.50

This paper has been typeset from a \LaTeX file prepared by the author.